CrossMark

ORIGINAL ARTICLE

Predicting chip and non-chip formation when micromachining Ti-6Al-4V titanium alloy

Mark J. Jackson[1] · Tamara Novakov[1] · Marcio Bacci da Silva[2] · Alisson R. Machado[2,3]

Abstract Mechanical micromachining is an alternative to standard methods of microfabrication owing to its applicability to a wide range of materials, cost, and versatility of the process. Many approaches have been undertaken to understand the behavior on such a small scale including experimental work, finite element analysis (FEA), molecular dynamics simulations (MD) as well as closed-form analytical approaches. The purpose of the present study investigated the use of Third Wave Systems' AdvantEdge™ Lagrangian-Eulerian formulated FEA software to analyze chip and non-chip formation when micromachining Ti6Al4V titanium alloy for medical device applications. For the specific machining conditions described in this paper, chip formation occurred when cutting force (F_C)/thrust force (F_T) > 1 and burr formation occurred when F_C/F_T < 1. In addition to the force conditions, when the ratio of feed per tooth to tool edge radius is approximately unity ($f_{tooth}/t_r \sim 1$), the micromachining process forms chips. When the ratio it decreased equal to 0.5 ($f_{tooth}/t_r = 0.5$), chip formation and burr formation exist simultaneously. However, when the ratio approaches an approximate value of 0.3 ($f_{tooth}/t_r \sim 0.3$), burr formation is dominant. The paper focuses on understanding the mechanisms of chip formation as a way to preserve the integrity of the surfaces of medical materials.

✉ Mark J. Jackson
jacksonmj04@yahoo.com; mjjackson@k-state.edu

[1] Center for Advanced Manufacturing, Purdue University, Indiana, USA

[2] LEPU/FEMEC, Federal University of Uberlandia, Uberlândia, MG CEP 38.400-902, Brazil

[3] Mechanical Engineering Graduate Program, Pontifícia Universidade Católica do Paraná—PUC-PR, Curitiba, PR CEP 80215-901, Brazil

1 Introduction

Micromachining of various materials including those materials used in medical devices such as titanium and its alloys has gained importance over the last several decades with the development of new fields of electronics, optics, aerospace applications, environmental sciences, communications, automotive design, die and mold design, medical devices, and biotechnology applications. Development of features as small as 1 μm and less is a common task for engineers and requires more attention for further process development if the emphasis is focused on further reductions in size. So far, micromachining has been mainly focused on the semiconductor industry where chemical etching has been the main process of interest. However, processes such as Lithography Electroforming Molding (LiGA), laser machining, ion beam machining, micro electro discharge machining, micromechanical machining, etc. are becoming widely applicable to developing products at many length scales. Micromechanical machining was developed as a bridge between nano and macrofeature development and is applicable for the production of individual parts rather than to batches of parts that are manufactured using other types of micromachining processes. Fabrication of free-form surfaces for the use in the production of microinjection molds is one of the new areas of application due to the interest in building MEMS and NEMS devices [1].

Micromachining differs from conventional machining, bringing with it a vast array of challenges. One of the main problems under investigation is the nature of chip formation

Springer

(and non-chip formation) and the development and control of surface features. This is mainly due to the "size effect" and the formation of severely negative rake angles imposed on the cutting tool during micromachining. The size effect is related to reaching a theoretical material strength value presented through the increase in specific energy with the decrease in the size of the uncut chip thickness. Owing to the fact that material homogeneity is not applicable to micromachining and because of the comparable size of the tool to microstructural features, the material reaches its theoretical strength at such a scale. Many researchers have tackled the problem of identifying causes of this phenomenon [2–6] and have connected it to a strengthening mechanism of the material owing to the decreasing number of defects in the microstructure of the machined material, thus increasing the strain rate at the primary shear zone, decreasing its thermal softening point, and inducing a strain gradient plasticity effect. Furthermore, with the decrease in the uncut chip thickness, the mechanism of chip formation changes from shearing to plowing-and-rubbing changing the force distributions and the energy consumed during chip and non-chip formation. The minimum uncut chip thickness value directly defines the quality of the surface obtained by the machining process indicating the importance of this parameter in micromachining.

The minimum chip thickness has been analyzed using various methods including cutting force periodicity [7], stress ratio derived from cutting and thrust forces [8], transition from interfacial sliding to microcutting [9], neutral point analysis [10], [11], effects of surface roughness [12], relationships between the friction coefficient, tool radius, and minimum chip thickness [13], molecular dynamics simulations [14] as well as traditional experimental work [15]. The research presented in this paper is focused on determining the transition from non-chip to chip formation using the cutting-to-thrust force ratio as the primary parameter in the determination of process mechanics. As the cutting force/thrust force ratio changes, the stability of the process also changes. Owing to the stringent requirements of producing medical implants using Ti6Al4V alloy with a defined surface quality, finite element modeling is used to simulate the effects of changing the cutting force/thrust force ratio, the ratio of feed per tooth/tooth edge radius, and their influences on chip and non-chip (burr) formation in the micromachining of Ti6Al4V titanium alloy, which has direct effect on surface quality and integrity.

2 Finite element model

In the finite element method, the material is represented using a continuum mechanics approach where the chemistry, crystal lattice, and grain size are neglected and the material is considered to be a continuum. The nodes and their number are determined arbitrarily and do not represent features of the material. The mesh parameters are set up in such a way that they only determine the sensitivity during the simulation by using a finer mesh when small feeds or depths of cut are used to capture features associated with micromachining. Finite element analysis (FEA) can be split into three groups: Lagrangian, Eulerian, and arbitrary Lagrangian-Eulerian methods. Lagrangian FEA is based on the assumption that the mesh is attached to the workpiece material and it moves with the material. Owing to the fact that the elements change shape, it is often necessary to use re-meshing to restore distorted elements and that adaptive re-meshing is more commonly used. Eulerian FEA involves a workpiece material which flows through the preset mesh fixed in space. There is no element distortion in this method. However, the chip formation cannot be modeled and only steady-state problems can be analyzed. Owing to the advantages and disadvantages of both methods, a combination of the two called arbitrary Lagrangian-Eulerian approach is more frequently used. For these reasons, a Lagrangian-Eulerian FEA was employed in the analysis.

The model used in the computational analysis of chip formation at the microscale is a three-dimensional Lagrangian-Eulerian formulated finite element model, which is an explicit dynamic model that is thermomechanically coupled used specifically for machining operations. The model uses adaptive re-meshing capable of finite resolutions at multiple length scales to incorporate cutting edge radius, the secondary shear zone, and chip loading effects. Multiple body deformation simulates tool–workpiece interactions in addition to transient thermal analyses. Finite deformation kinematics and updated stress conditions have been formulated by Third Wave Systems that include balancing linear momentum and calculating thermal conditions using the second law of thermodynamics.

For the *kinematic conditions*, the balance of linear momentum is:

$$\sigma_{ij,j} + \rho b_i = \rho \ddot{u}_i \tag{1}$$

The principle of virtual work in its weakest form is stated:

$$\int_B v_i \sigma_{ij,j} + v_i \rho b_i dV = \int_B \rho v_i \ddot{u}_i dV \tag{2}$$

Integration by parts and rearranging the terms provide the force balance for the system:

$$\int_B \rho v_i \ddot{u}_i dV + \int_B v_{i,j} \sigma_{i,j} dV = \int_{\partial B} v_i \sigma_{i,j} n_j d\Omega + \int_B v_i \rho b_i dV \tag{3}$$

In other terms:

(Inertial terms) + (Internal forces) = (External forces) + (Body forces), or when expressed in matrix format:

$$\boldsymbol{M}\boldsymbol{a}_{a+1} + \boldsymbol{R}_{n+1}^{\text{int}} = \boldsymbol{R}_{n+1}^{\text{ext}} \tag{4}$$

Where,

$$M_{ab} = \int_{B0} \rho_0 N_a N_b dV_o \qquad (5)$$

Here, M_{ab} is the mass matrix and the external force array, R_{ia}, is:

$$R_{ia}^{\text{ext}} = \int_{B0} b_i N_a dV_o + \int_{\partial B0\tau} \tau_i N_a d\Omega_o \qquad (6)$$

And the internal force array is:

$$R_{ia}^{\text{int}} = \int_{BO} P_{i,j} N_{a,j} dV_o \qquad (7)$$

It should be noted that N_a, $a = 1.....n,u,m,p$ are shape functions, the repeated indices imply summation, a comma (,) represents a partial differentiation with respect to the spatial coordinate, and $P_{i,j}$ is the nominal stress known as the Piola-Kirchhoff stress tensor.

For the thermal conditions, heat generation and transfer are derived using the second law of thermodynamics. A weak form of the first law of thermodynamics (in discretized form) is:

$$CT_{n+1} + KT_{n+1} = Q_{n+1} \qquad (8)$$

A lumped capacitance matrix, **C**, is used in this case to eliminate the need for solving equations, thus:

$$CT + KT = Q \qquad (9)$$

Where, **T**, is an array of temperature nodes and the heat capacity matrix is:

$$C_{ab} = \int_{Bt} c\rho N_a N_b dV_o \qquad (10)$$

The heat conductivity matrix is:

$$K_{ab} = \int_{B0} D_{i,j} N_{a,i} N_{b,j} dV \qquad (11)$$

The heat source array assumes that the chip, or tool, has the appropriate value of h:

$$Q_a = \int_{Bt} s N_a dV + \int_{B\tau q} h N_a dS \qquad (12)$$

During micromachining processes, the sources of heat are chip formation (plastic deformation) and frictional sliding at the tool–workpiece interface. The rate of heat generated is:

$$s = \beta \cdot \dot{W}^{\text{p}} \qquad (13)$$

where, $\dot{W}^{\text{p}}$ is the power consumed in plastic deformation per unit deformed volume and the Taylor-Quinney coefficient, $\beta \sim 0.9$. The rate of heat generated at the frictional contact zone is:

$$h = -\boldsymbol{t}.\|\boldsymbol{v}\| \qquad (14)$$

where $\boldsymbol{t}$ is the traction at the contact zone and $\boldsymbol{v}$ is the velocity across the contact zone. In order to use the finite element model to simulate the conditions of micromachining Ti6Al4V titanium alloy, an appropriate material model is required to properly simulate machining conditions. For this reason, a custom power law constitutive material model was used.

3 Constitutive material model

Computational analysis was conducted using Third Wave Systems' AdvantEdge™ FEA software. The software utilizes a custom power law constitutive material model incorporating strain hardening effects, strain rate sensitivity, thermal softening effects, and a damage model. Thus,

$$\sigma(\varepsilon^p, \dot{\varepsilon}, T) = g(\varepsilon^p) \times \Gamma(\dot{\varepsilon}) \times \Theta(T) \qquad (15)$$

where, σ is the stress as function of strain hardening, strain rate sensitivity, and temperature, $g(\varepsilon^p)$ accounts for strain hardening, $\Gamma(\dot{\varepsilon})$ accounts for strain rate sensitivity, and $\Theta(T)$ accounts for thermal softening of the cut material.

Strain hardening shows the dependence of the flow stress on strain and is incorporated into the finite element model as:

$$g(\varepsilon^p) = \sigma_0 \left[1 + \frac{\varepsilon^p}{\varepsilon_0^p}\right]^{\frac{1}{n}} \text{ if } \varepsilon^p < \varepsilon_{\text{cut}}^p \qquad (16)$$

$$g(\varepsilon^p) = \sigma_0 \left[1 + \frac{\varepsilon_{\text{cut}}^p}{\varepsilon_0^p}\right]^{\frac{1}{n}} \text{ if } \varepsilon^p \geq \varepsilon_{\text{cut}}^p \qquad (17)$$

where, σ_0 the initial yield stress, ε^p is the plastic strain, ε_0^p is the reference plastic strain, $\varepsilon_{\text{cut}}^p$ is the cutoff strain, and n is the strain hardening exponent. Thermal softening parameters have been defined using the following equations:

$$\Theta(T) = c_0 + c_1 T + c_2 T^2 + c_3 T^3 + c_4 T^4 + c_5 T^5 \text{ if } T < T_{\text{cut}} \qquad (18)$$

$$\Theta(T) = \Theta(T_{\text{cut}}) \left(1 - \frac{T - T_{\text{cut}}}{T_{\text{melt}} - T_{\text{cut}}}\right) \text{ if } T \geq T_{\text{cut}} \qquad (19)$$

where, c_0 to c_5 are coefficients of the polynomial fit, T is the temperature, T_m is the melting temperature, and T_{cut} is the linear cutoff temperature. Strain rate sensitivity is presented as the dependence of the flow stress on strain defined using the following equations:

$$\Gamma(\dot{\varepsilon}) = \left(1 + \frac{\dot{\varepsilon}}{\dot{\varepsilon}_0}\right)^{\frac{1}{m_1}} \text{if } \dot{\varepsilon} \leq \dot{\varepsilon}_t \tag{20}$$

$$\Gamma(\dot{\varepsilon}) = \left(1 + \frac{\dot{\varepsilon}}{\dot{\varepsilon}_0}\right)^{\frac{1}{m_2}} \left(1 + \frac{\dot{\varepsilon}_t}{\dot{\varepsilon}_0}\right)^{\left(\frac{1}{m_1} - \frac{1}{m_2}\right)} \text{if } \dot{\varepsilon} > \dot{\varepsilon}_t \tag{21}$$

where, $\dot{\varepsilon}$ is the strain rate, $\dot{\varepsilon}_0$ is the reference plastic strain rate, $\dot{\varepsilon}_t$ is the strain rate of the transition between the high and low strain sensitivity, and m_1 and m are the low and high strain rate sensitivity indices, respectively.

The damage model is expressed using the equation:

$$D = \sum_i \frac{\Delta \varepsilon_i^p}{\varepsilon_{fi}^p} \tag{22}$$

where, D is the dimensionless cumulative damage, $\Delta \varepsilon_i^p$ is the instantaneous increment of strain, and ε^p_{fi} is the instantaneous strain to failure. Constants applied in the power law constitutive material model are presented in Table 1.

The numerical values shown in Table 1 reflect the works of many researchers and their effort to capture the properties of simulating the machining of Ti6Al4V titanium alloy. However, for the experiments noted here, some constants are calculated and some selected as arbitrary measures. Therefore, caution should be observed when making absolute interpretations of the computational data presented in this paper. The next sections of the paper are focused on using the finite element modeling technique to analyze chip formation mechanisms and ensure that the correct chip formation regime is selected that will improve surface quality and integrity of the micromachined medical material.

4 Computational results

4.1 Cutting forces and chip formation

Initial studies in the area of modeling of the micromachining process established the use of finite element software for simulating the micromilling process in the up-cut and down-cut milling regimes [1, 2, 7, 12]. The geometry of the end view of the cutting edge of the micromilling tool looks very similar to the adjacent view of a standard lathe cutting tool, the difference being that one tooth of the milling cutter is simulated and the curvature of the chip formed is so small it appears as though the workpiece is perpendicular to the motion of the cutting edge of the tooth. In the practical machining process,

each tooth cuts a piece of the workpiece material, but the FEA model simulates the cutting associated with one tooth in contact with the workpiece material. The validity of simulating the cutting of material using one tooth is shown in Fig. 1. The six-tooth micromilling cutter shows the chip flow direction in addition to the local geometry of one tooth (Fig. 1a, b). Here, the flow of chip material over the flank face of a cutting edge of a single tooth can be simulated in two dimensions using the Third Wave Systems' AdvantEdge™ FEA software using the down-cut milling regime. The simulations presented in this paper consider on edge of one tooth of the milling cutter (Fig. 1c) and the path of material flow shown in the simulations is a replica of the material flow shown in Fig. 1d, where the flow of the chip is abruptly redirected due to the tooth's contact between the workpiece material and the tool edge radius. The applicability of the use of the FEA modeling technique has been verified by various researchers detailed in the reference section of this paper [1, 2, 7, 12]. A conventional force analysis was compared to computational finite element models of the micromachining process, and the accuracy of using such analysis was validated with various materials, tool materials and coatings, and machining parameters. In terms of forces, radial (dF_r) and tangential forces (dF_t) for an elemental chip at the microscale are:

$$dF_r = \frac{K_t R}{\tan\alpha} K_r t_c(\theta) d\theta \tag{23}$$

$$dF_t = \frac{K_t R}{\tan\alpha} t_c \theta \, d\theta \tag{24}$$

where, K_t is the average cutting pressure constant, K_r is the ratio of the radial and tangential cutting force, R is the radius of the cutting tool, α is the helix angle, θ is the angular position of the cutter, and t_c is the instantaneous uncut chip thickness given as:

$$t_c = t_x \sin\theta - \frac{N}{2\pi R} t_x^2 \sin\theta\cos\theta + \frac{1}{2R} t_x^2 \cos^2 t \tag{25}$$

where, t_x is the feed and N is the spindle speed in revolutions per minute. Resolving the forces into horizontal (dF_x) and vertical (dF_y) directions yields:

$$dF_x = \frac{K_t r}{\tan\alpha} t_c(\theta)[\cos\theta d\theta + K_r \sin\theta d\theta] \tag{26}$$

$$dF_y = \frac{K_t R}{\tan\alpha} t_c(\theta)[\sin\theta d\theta - K_r \cos\theta d\theta] \tag{27}$$

Integrating Eqs. 26 and 27 and finding the forces in the directions give:

$$\begin{pmatrix} F_x \\ F_y \end{pmatrix} = \frac{t_x R}{2\tan\alpha} \begin{bmatrix} P_1 & P_2 \\ P_2 & -P_1 \end{bmatrix} \begin{pmatrix} K_t \\ K_t K_r \end{pmatrix} \tag{28}$$

Table 1 Constants applied to the power law constitutive material model

Parameter	Designation	Value	Reference
Thermal conductivity (W/m °C)	k	7.3	[16]
Heat capacity (J/kg °C)	C	580	[16]
Coefficient of thermal expansion (1/°C)	α	0.970×10^{-5}	[17]
Density (kg/m³)	ρ	4430	[17]
Initial yield stress (Pa)	σ_0	0.98×10^9	[16]
Strain hardening exponent	n	30.9	Calculated
Reference plastic strain	ε_0^p	0.0125	[18]
Cutoff strain	ε_{cut}^p	10^4	[18]
Coefficient	C_0	999.72	Calculated
Coefficient	C_1	−0.8785	Calculated
Coefficient	C_2	−0.0141	Calculated
Coefficient	C_3	9E-0.5	Calculated
Coefficient	C_4	−2E-0.7	Calculated
Coefficient	C_5	1E-10	Calculated
Reference temperature °C	T_r	27	Arbitrary
Cutoff temperature °C	T_{cut}	1000	[19]
Low rate exponent	m_1	72	Calculated
High rate exponent	m_2	72	Calculated
Reference strain rate (1/s)	$\acute{\varepsilon}^0$	1	[20]
Threshold strain rate (1/s)	$\acute{\varepsilon}_t$	10^6	[21]
Young's modulus (Pa)	E_y	$1.1E^{11}$	[16]
Poisson's ratio	Pr	0.41	[16]
Coefficient	D_0	11.292	Calculated
Coefficient	D_1	−0.0114	Calculated
Coefficient	D_2	4E-0.5	Calculated
Coefficient	D_3	−5E-08	Calculated
Coefficient	D_4	−2E-10	Calculated
Coefficient	D_5	4E-13	Calculated
Damage cutoff temperature °C	T_c	500	[22]
Failure strain increment	ε_{fi}^p	0.1	Arbitrary

Where,

$$P_1 = \left[\sin^2\theta + \frac{N}{\pi R}t_x\frac{\cos^3\theta}{3} + \frac{t_x}{R}\left(\sin\theta - \frac{\sin^3\theta}{3}\right)\right]_{\theta_1}^{\theta_2} \quad (29)$$

$$P_2 = \left[\theta - \frac{\sin2\theta}{2} - \frac{N}{\pi R}\frac{\sin^3\theta}{3} - \frac{t_x}{R}\frac{\cos^3\theta}{3}\right]_{\theta_1}^{\theta_2} \quad (30)$$

where, K_r and K_t are constants that are material specific. From their analyses, references [1, 2, 7, 12] report that their finite element formulations of cutting forces maintained close accuracy to the closed-form solutions of forces shown by Eq. 28. Their work thus validated the use of finite element formulations to the solution of forces in micromachining with milling cutters.

The machining parameters simulated in the study include variable rotational cutting speeds, variable feed/tooth, variable tool edge radii, and variable tool materials. Rotational speeds used in the simulations are 100,000, 150,000, and 200,000 rpm, respectively. The tool edge radius values used are 10 and 4 μm, respectively. The feed/tooth values used for the 10-μm tool edge radius are 10, 5, and 3.125 μm, while for the 4-μm tool edge radius, the values are 4, 2, and 1.25 μm, respectively. The tool material used for the simulations includes a cemented tungsten carbide cutting tool (with some coated with diamond) with six equi-spaced cutting teeth (Fig. 1). The rake angle of the edge of each tooth was 5° and the relief angle was 10°. The workpiece material used for the simulations was a Ti6Al4V medical grade alloy (α+β type alloy) with the following mechanical properties: tensile strength (895–930 MPa), yield strength (825–869 MPa), elongation percent (6–10 %), and elastic modulus of 110–114 GPa. α+β Ti alloys include alloys with enough α- and β-stabilizers to expand the α+β phase field to exist at

Fig. 1 Six-tooth micromilling cutter manufactured from tungsten carbide showing **a** the end view of the cutter, **b** a magnified image of one tooth of the cutter showing tool edge radius and the remnants of folded chip material that has adhered to the flank face of the cutting edge, **c** global view of the tips of the teeth, and **d** a magnified image of the tool edge radius and flow of the chip over the flank face of the cutting edge [26]
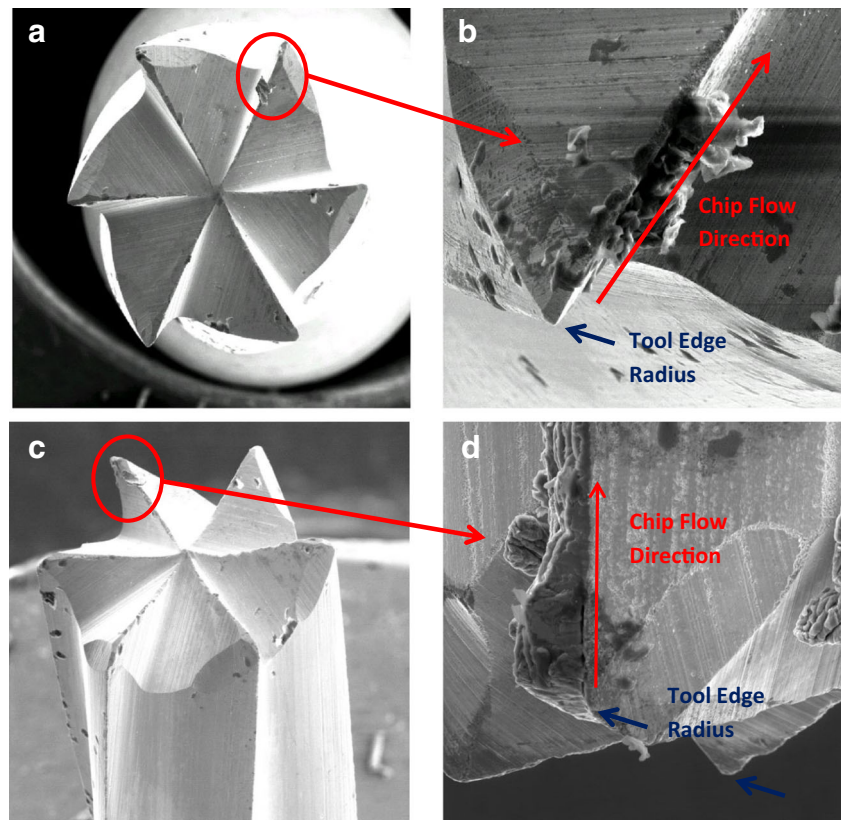
room temperature. The α- and β-phase combination allows one to obtain an optimum balance of mechanical properties, the characteristics of which may be tailored by applying the correct heat treatments and thermomechanical processing regimes. Owing to its malleability and enhanced mechanical behavior at low temperatures, Ti6Al4V is used as a biomaterial mainly in orthopedic implant devices.

Finite element simulations of the micromachining process are shown in Figs. 2, 3, 4, 5, 6, 7, 8, 9, and 10 and Tables 2, 3, 4, 5, 6, and 7. When analyzing the results obtained for chip curl and temperature as shown in Figs. 2, 3, 4, 5, and 6, it has become obvious that there is a change in the chip shape as the ratio of feed per tooth (depth of cut) and tool edge radius (f_{tooth}/t_r) changes. Furthermore, as the uncut chip thickness is decreased, the bending moment acting on the chip root changes the direction of the cut chip. For the ratio of feed per tooth/tool edge radius that is close to unity ($f_{tooth}/t_r \sim 1$), the bending moment acts at the chip root, moving the chip away from the tool. As the ratio of feed per tooth/tool edge radius is decreased to 0.5 ($f_{tooth}/t_r = 0.5$), the bending moment is absent and the chip moves vertically in an upward direction. As the ratio of the feed per tooth/ tool edge radius is further decreased to ~0.3 ($f_{tooth}/t_r \sim 0.3$), an opposite bending moment bends the chip towards the cutting tool.

The change in the feed per tooth/ tool edge radius ratio (f_{tooth}/t_r) also produces a change in the ratio of maximum cutting/thrust forces (F_C/F_T). As the chip thickness is decreased in the "down-cut milling" process, the cutting/thrust

force ratio changes and is presented in Figs. 7, 8, 9, and 10. The transition from $F_C/F_T < 1$ (burr formation) to $F_C/F_T > 1$ (chip formation) defines a transition from burr-to-chip formation and is further characterized in Tables 2, 3, 4, 5, 6, and 7 using rations, F_C/F_T and f_{tooth}/t_r, for the simulations presented in this study.

The change in the ratio of cutting and thrust forces has been confirmed by Kang et al. [23] showing that during the micromachining process, force components accounting for plowing and sliding increase with the decrease in uncut chip thickness, which leads to a change in the force distribution. As opposed to macromilling processes where the thrust force reaches a maximum level ~30 % of the maximum cutting force, the radius of the edge of the tool approaches the size of the uncut chip thickness in micromilling processes, which causes the thrust force to become higher than the cutting force. Consequently, a change in the ratio of thrust-to-cutting force occurs. The change in force is shown to trigger the transition from cutting to plowing and vice versa [23].

4.2 Influence of machining parameters on cutting and thrust force

4.2.1 Spindle speed effect

When analyzing the effect of the spindle speed on cutting and thrust forces when machining Ti6Al4V titanium alloy at the

Fig. 2 Contour comparison for 10 μm tool edge radius cutting tooth machining at **a** 10 μm feed per tooth, **b** 5 μm feed per tooth, and **c** 3.125 μm feed per tooth using a tungsten carbide cutting tool. The spindle speed is 100,000 rpm and the maximum temperature in cutting the chip is ~68, 41, and 57 °C, respectively
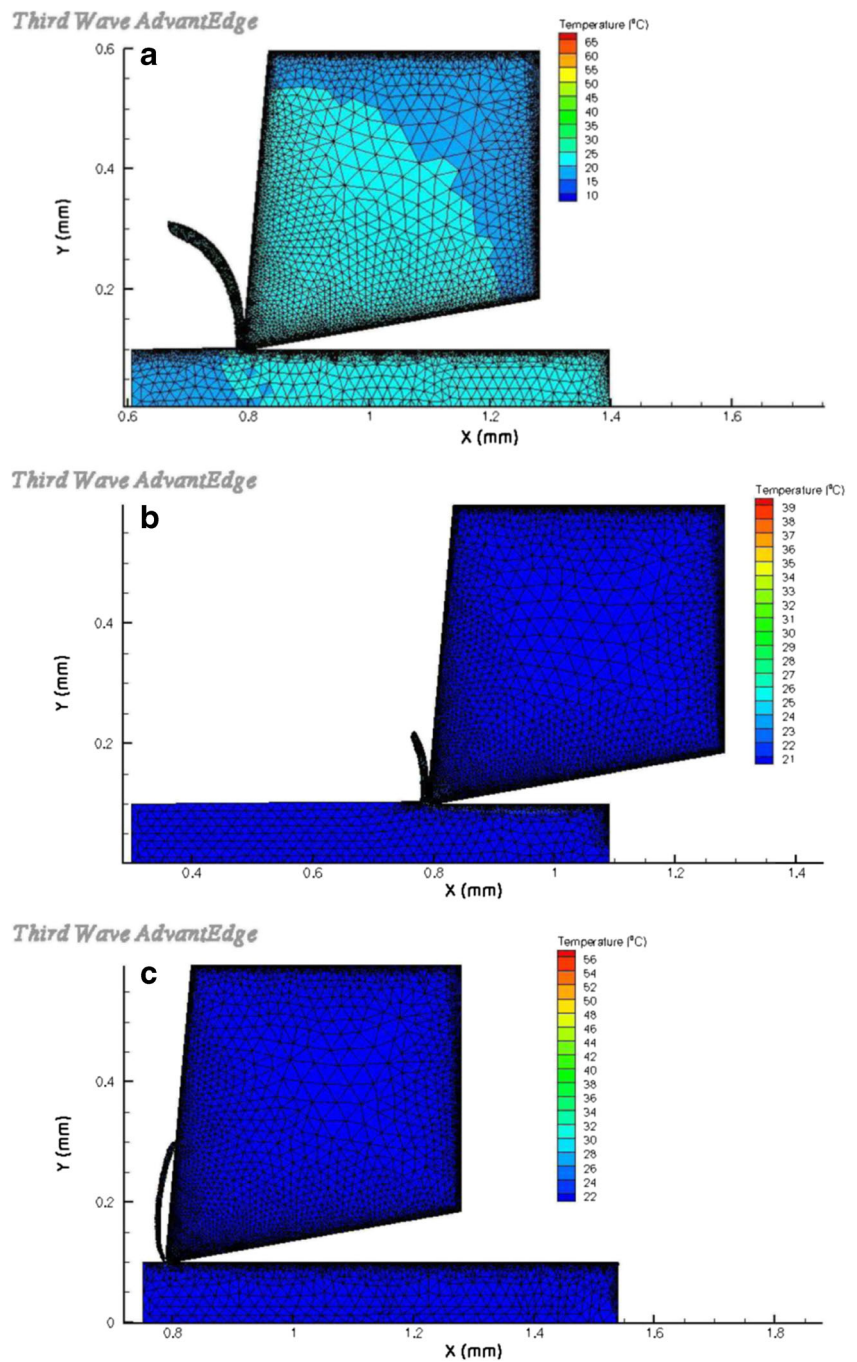

macroscale, it is apparent that there is a significant change in force when increasing the rotational speed. As the value for the rotational speed increases, the thrust force values show a direct dependence yielding higher values [24]. The rise in the thrust force with the increase in rotational speed is attributed to the adherence of the chip to the cutting tool, which is a characteristic associated with the machining of Ti alloys at the macroscale. As the cutting speed increases when machining Ti alloys, the temperature at the tool/workpiece interface increases to several hundred degrees Celsius [25]. With the increase in temperature, adherence of the chip to the tool is promoted. The degree of adherence is considered to increase with the increase in speed due to the increase in temperature, eventually resulting in the increase in thrust force. However, it has been determined by Robinson [26] that temperatures in micromachining commonly used engineering materials are very low, and when micromachining Ti6Al4V titanium alloy, the temperature stabilizes at ~25 °C depending upon the machining parameters. Therefore, the fact that there is a lack of sustained heat flow at high temperatures allows one to predict

Fig. 3 Contour comparison for 4 μm tool edge radius cutting tooth machining at **a** 4 μm feed per tooth, **b** 2 μm feed per tooth, and **c** 1.25 μm feed per tooth using a tungsten carbide cutting tool. The spindle speed is 100,000 rpm and the maximum temperature in cutting the chip is ~25, 25, and 25.5 °C, respectively
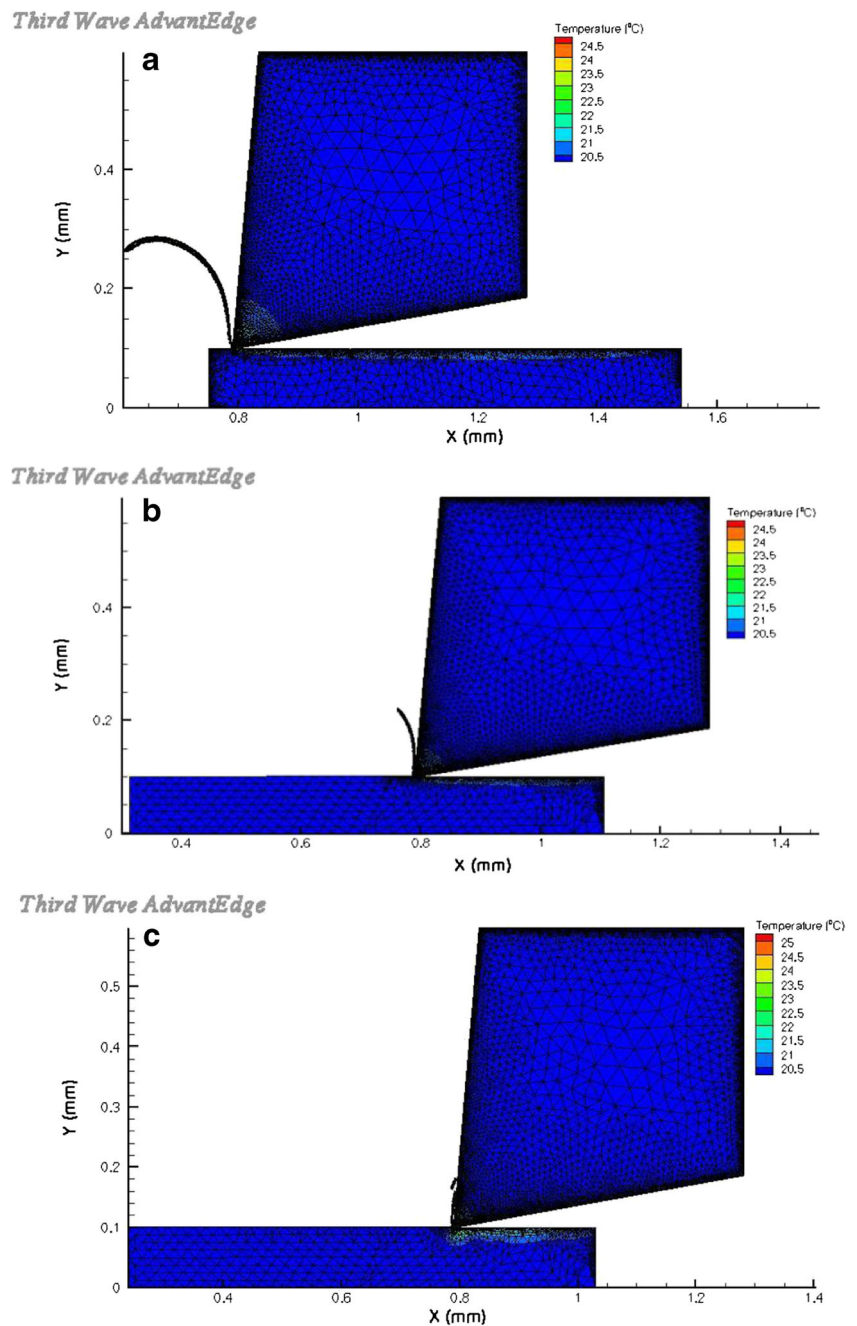
that the chips generated during micromachining do not actually adhere to the cutting tool, and consequently thrust forces do not change with an increase in the rotational speed of the cutting tool. The stability in computed magnitudes of forces with the consequent change in the rotational speed is presented in Figs. 11 and 12. For the tungsten carbide tools, the forces are relatively stable at the three magnitudes of cutting feeds. For diamond tools, the cutting forces are relatively stable, while the thrust force shows some level of stability that could be attributed to difference in hardness between using tungsten carbide and diamond as the tool material.

4.2.2 Effect of feed per tooth

The influence of the feed per tooth when micromachining Ti6Al4V titanium alloy is significant in terms of cutting and thrust forces. The point at which the forces are equal is used to define the stability of the process and the recommended parameters in terms of feed per tooth, tool diameter, and spindle speed. It is shown in Figs. 13 and 14 that both cutting and thrust forces increase with the increase in the feed/tooth. The transition point defines three stages of machining: (A) burr formation, (B) mixed mode region, and (C) chip formation.

Fig. 4 Contour comparison for 10 μm tool edge radius cutting tooth machining at **a** 10 μm feed per tooth, **b** 5 μm feed per tooth, and **c** 3.125 μm feed per tooth using a tungsten carbide cutting tool. The spindle speed is 150,000 rpm and the maximum temperature in cutting the chip is ~27, 47, and 29 °C, respectively
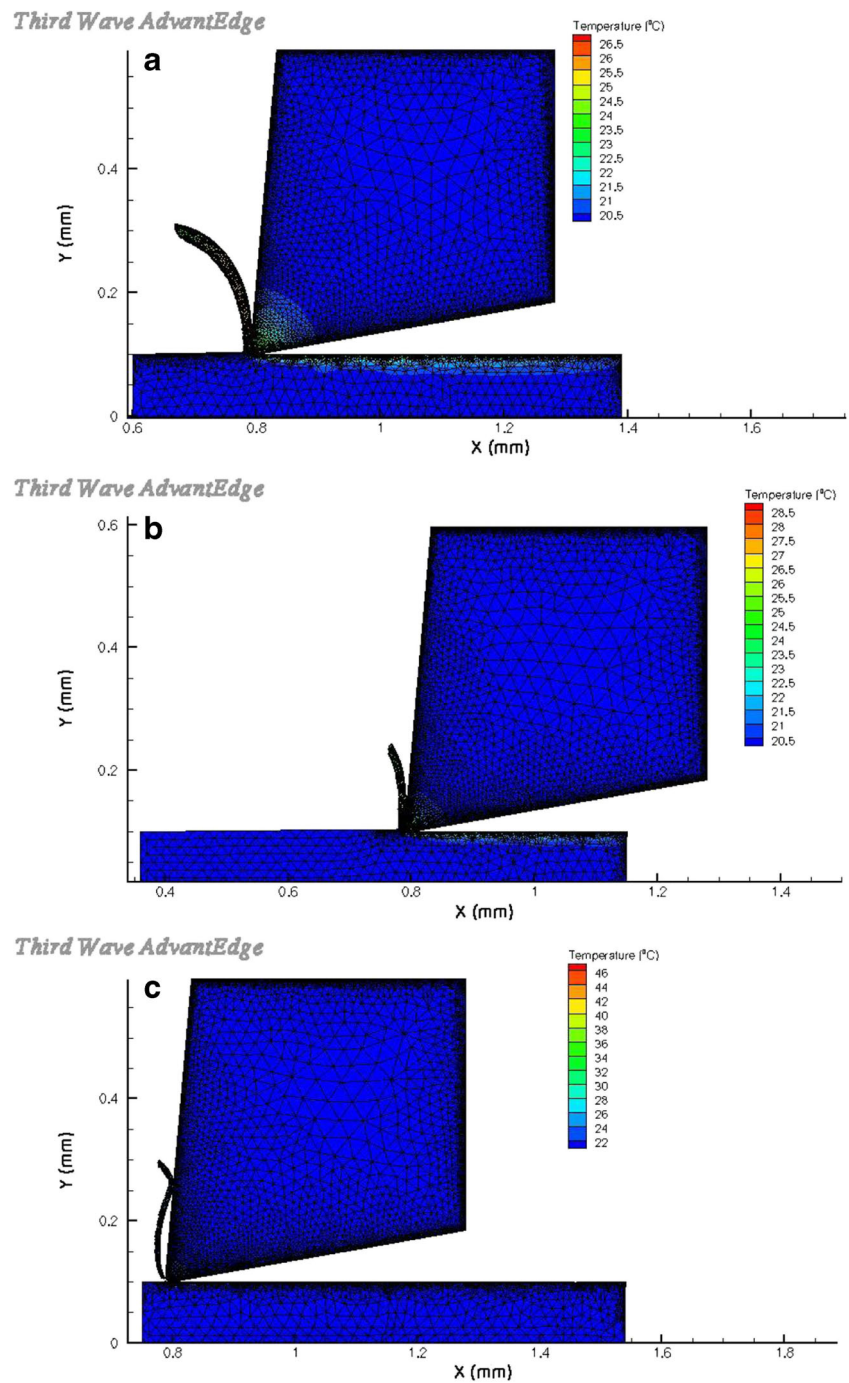
There is a strong similarity when the results are compared with the results demonstrated by Kim and Kim [27] who had based their research on the differentiation of micro and macrocutting processes.

Their research shows that the trend of the force increase with the depth of cut is accounted for by three components of the force: the rake face which is the equivalent to the cutting force in macromachining, the clearance face which is a consequence of the contact of the workpiece, and the tool clearance face due to the elastic spring back of the workpiece material and the round edge of the tool.

4.3 Changes in heating rate

When the change in heating rate at the point where $F_C = F_T$ is analyzed, there is a transition of forces from $F_C/F_T < 1$ to $F_C/F_T > 1$. When $F_C/F_T < 1$, burr formation is predominant and when $F_C/F_T > 1$, the chip formation is prevalent. It can be seen

Fig. 5 Contour comparison for 4 μm tool edge radius cutting tooth machining at **a** 4 μm feed per tooth, **b** 2 μm feed per tooth, and **c** 1.25 μm feed per tooth using a tungsten carbide cutting tool. The spindle speed is 150,000 rpm and the maximum temperature in cutting the chip is ~29, 25, and 26 °C, respectively
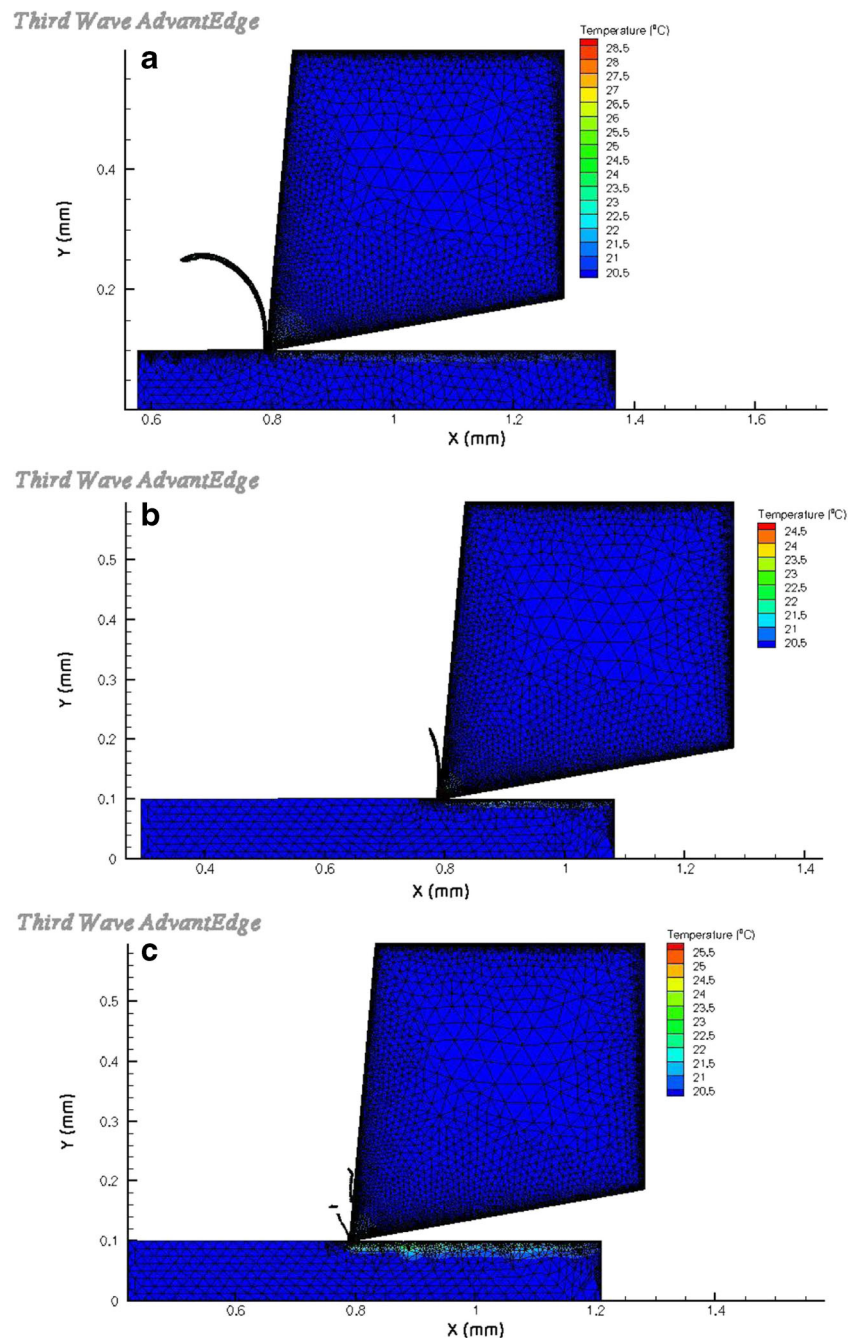

from Figs. 15, 16, 17, 18, 19, 20, 21, 22, 23, 24, 25, and 26 that there is a drastic difference in the shape and position of the thermal field. The heating rate field changes direction when there is a change from burr formation to chip formation. Before the transition, i.e., when stable machining and chip formation is present, the heating rate field is located in the chip root showing that the heat will dissipate into the chip rather than into the workpiece. The heat is then taken away by the chips from the tool and workpiece. It can be seen that the highest heating rate occurs at the chip root and is concentrated in one area with no distinctive dissipation path identified. Upon crossing into the region of burr formation, the heating rate field can be seen to move away from the free surface of the chip towards the tool and under the tool into the workpiece. Rather than going into the burr, the heat is partitioned into the workpiece. The partitioned heat could be considered responsible for the re-welding of the cracks in the burrs as it is pushed out of the tool–work material contact zone. It can be seen that the highest heating rate covers a larger area below the tool as well as below the chip root into the bulk of the work material. This change in the position of the heat rate field is expected to occur and is in accordance with the phenomena associated with the burr-to-chip transition [26].

Fig. 6 Contour comparison for 10 μm tool edge radius cutting tooth machining at **a** 10 μm feed per tooth, **b** 5 μm feed per tooth, and **c** 3.125 μm feed per tooth using a tungsten carbide cutting tool. The spindle speed is 200,000 rpm and the maximum temperature in cutting the chip is ~53, 29, and 31 °C, respectively
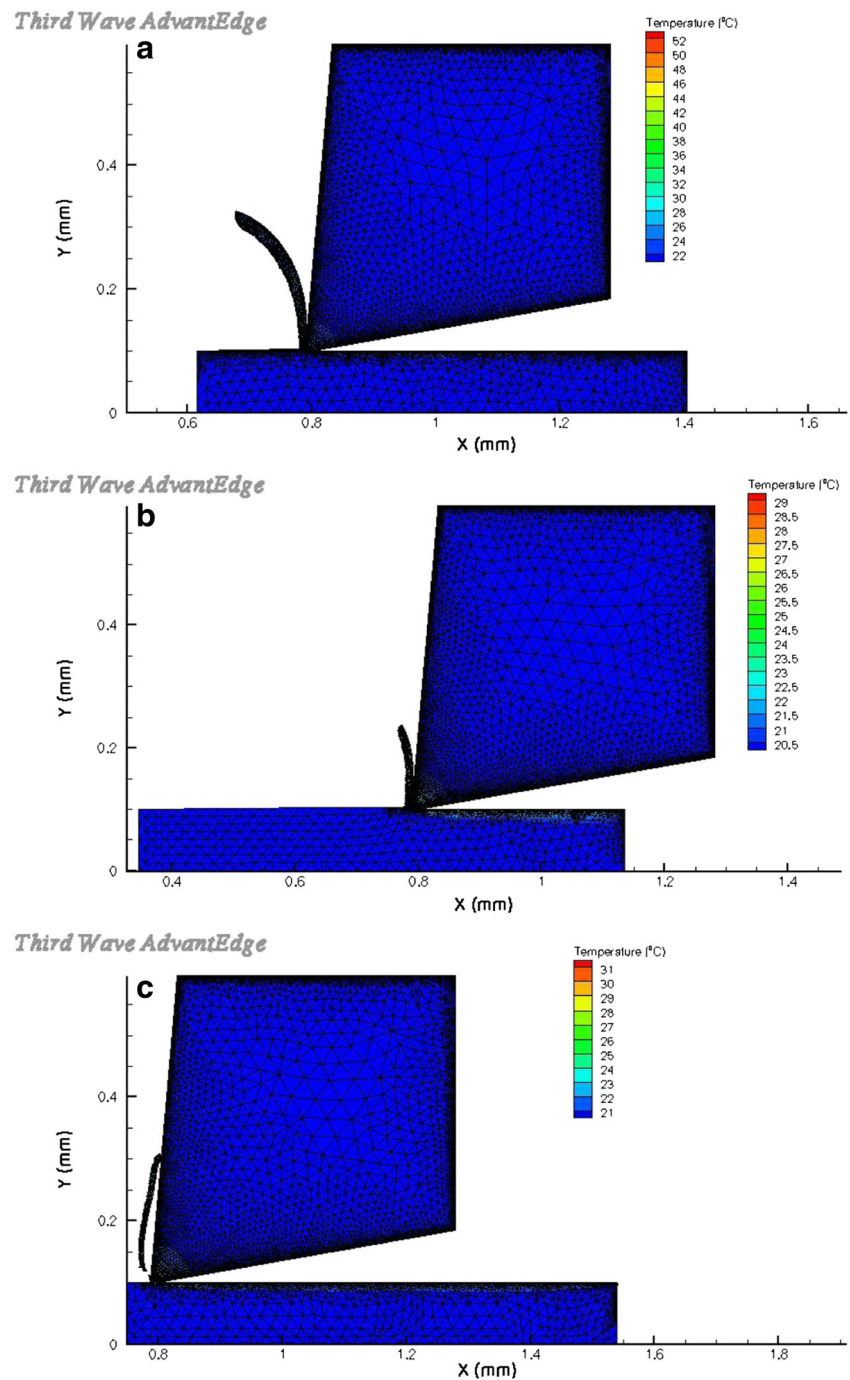
5 Discussion

5.1 Cutting forces and chip formation

The effect of the tool edge radius has been an important one throughout the investigations conducted in the finite element modeling of the machining process. Analysis has been conducted on the effect of edge roundness on stress and temperature when micromachining AISI 4340 steel using carbide tools using an arbitrary Lagrangian-Eulerian method [28].

Researchers simulated material flow around the tool edge without re-meshing or using a chip separation criterion and argue that this way of conducting FEA gives better predictions for machining-induced stresses [28]. Li and Shi [29] investigated the effect of the cutting edge radius on forces, chip thickness, and tool temperature. Owing to the less effective cutting with a large radius tool, the resulting cutting forces increase with the increase in the tool edge radius. The chip thickness is influenced somewhat by the increase in the tool edge radius showing slight increasing trend. An increasing

Fig. 7 Contour comparison for 4 μm tool edge radius cutting tooth machining at **a** 4 μm feed per tooth, **b** 2 μm feed per tooth, and **c** 1.25 μm feed per tooth using a tungsten carbide cutting tool. The spindle speed is 200,000 rpm and the maximum temperature in cutting the chip is ~26, 28.5, and 25 °C, respectively
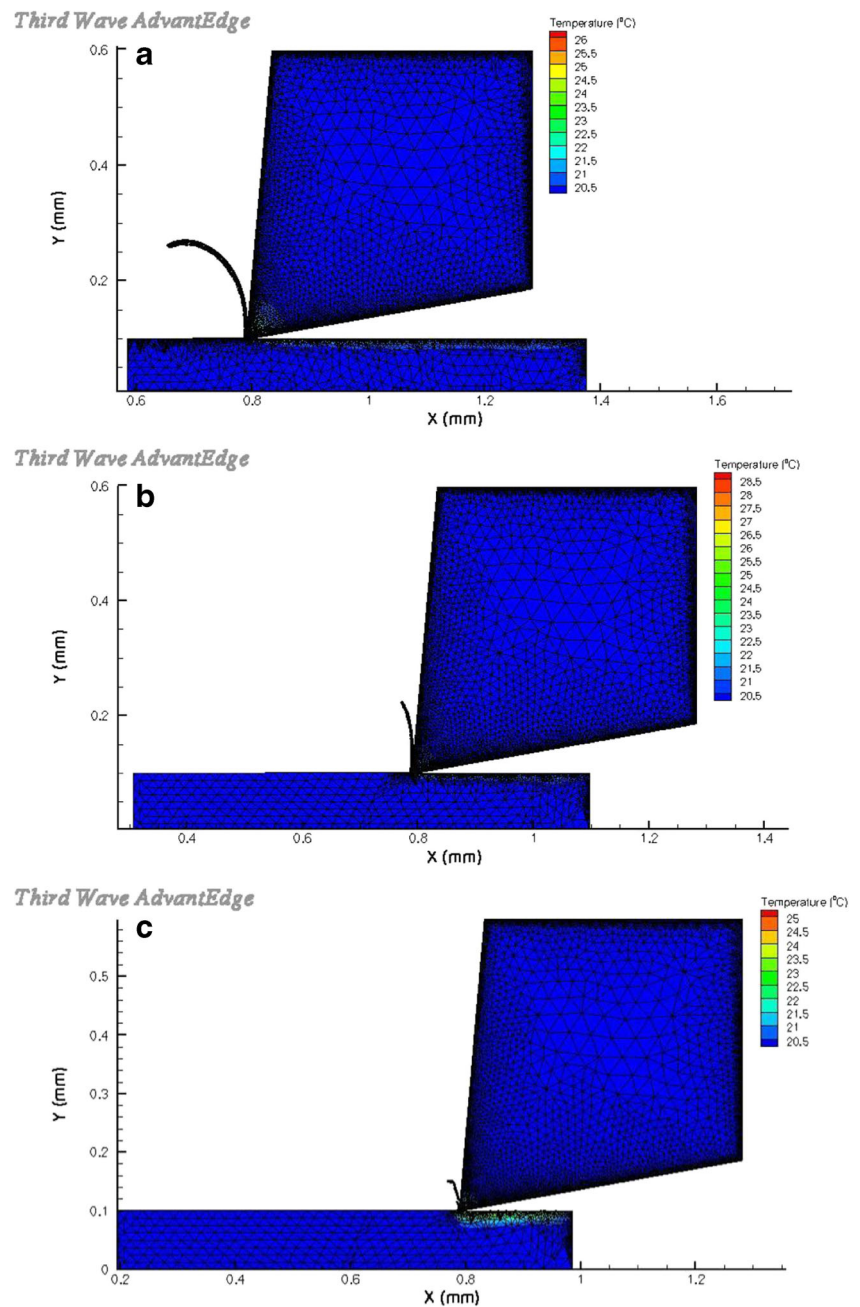
trend for tool temperature is observed with the increase in tool edge radius. In the present work, Figs. 2, 3, 4, 5, 6, and 7 show similar trends. When the tool nose radius is increased from 4 to 10 μm, the temperature at the tool tip is slightly elevated (Figs. 8, 9, and 10). Also noted is the slight increase in cutting force when the edge radius is increased. These observations are in agreement with the observations of similar finite element models [26, 28, 29]. The change in the ratio of cutting and thrust forces has been confirmed by Kang et al. [23] showing that during the micromachining process, force components accounting for plowing and sliding increase with the decrease in uncut chip thickness, which leads to a change in

the ratio of force distribution. When the radius of the edge of the tool approaches the size of the uncut chip thickness in micromilling process, the F_T becomes higher in magnitude than the F_C. Consequently, a change in the ratio of thrust-to-cutting force occurs because a transition from cutting to plowing takes place [23].

The mechanism of chip formation and chip morphology has been investigated by a number of authors who compared the simulated results with the experimentally obtained chips in order to understand chip formation micromachining various materials. A finite element analysis has been presented for both conventional and high speed machining of Ti6Al4V

Fig. 8 Cutting and thrust forces for **a** 10 μm tool edge radius and 5 μm feed rotating at 100,000 rpm spindle speed using a tungsten carbide cutting tool and **b** 4 μm tool edge radius and 4 μm feed rotating at 100,000 rpm spindle speed using a tungsten carbide cutting tool. The figures show the transition from burr-to-chip formation and the associated magnitude of force ratio
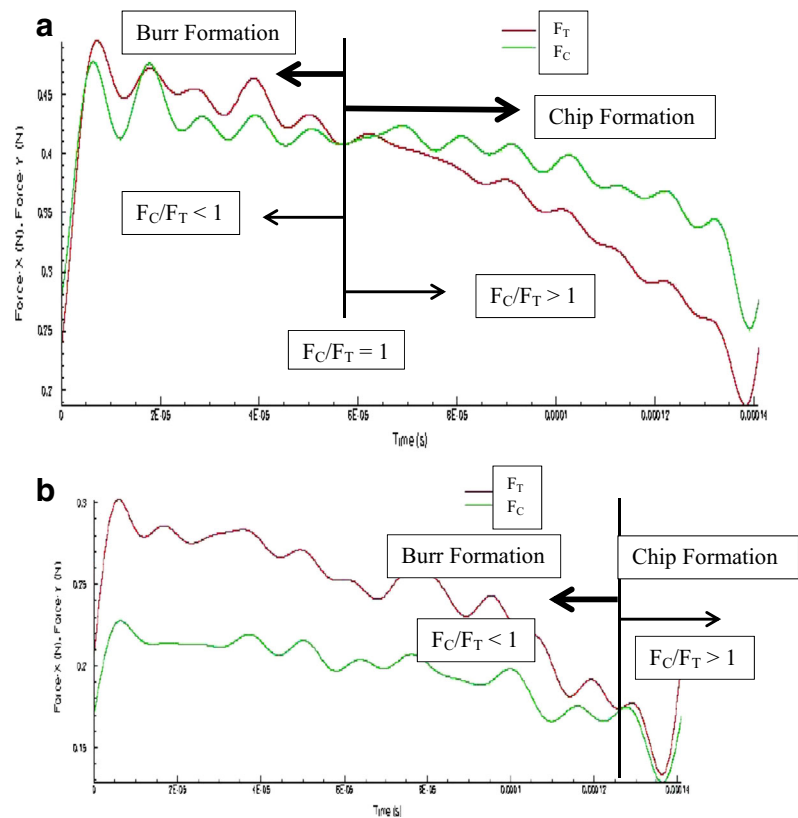

alloys incorporating the Johnson-Cook and the applied models [26, 30]. The researchers investigated chip formation and morphology and compared it to experimentally generated chips. The computational predictions were almost identical to experimentally generated chips. Of course, different material models produce slightly different curvatures of the chips, but the computed shapes are largely accurate when compared to the production of chips during micromachining. The verification of applying FEA principles to chip formation and morphology is validated by prior investigations [26, 30]. In the present work, by observing Figs. 2, 3, 4, 5, 6, and 7, it is obvious that there is a change in the chip shape as the ratio of feed per tooth and tool edge radius (f_{tooth}/t_r) changes in magnitude. Furthermore, as the uncut chip thickness is decreased, the bending moment acting on the chip root changes the direction of the cut chip. For a ratio of feed per tooth/tool edge radius that is close to unity ($f_{tooth}/t_r \sim 1$), the bending moment acts at the chip root, moving the chip away from the tool. As the ratio of feed per tooth/tool edge radius is decreased to 0.5 ($f_{tooth}/t_r = 0.5$), the bending moment is absent and the chip moves vertically in an upward direction. As the ratio of the feed per tooth/tool edge radius is further decreased to approximately 0.3 ($f_{tooth}/t_r \sim 0.3$), an opposing bending moment bends the chip towards the cutting tool. The same observations were made in previous investigations [26, 28, 29]. Obikawa and Usui [31] have focused their research on implementing a crack growth criterion into finite element

modeling to better predict discontinuous chip formation. They incorporated a fracture strain criterion and obtained results in very close agreement to the experimental findings. The influence of the chosen material model for the FEA on chip formation has been further investigated [32]. The choice of the model will clearly make a difference when interpreting the chip morphology results and comparing them with the experimentally obtained shapes. The chip curl radius can be observed to be different for each material model, and it is argued that the power law model provides the values closest to the experimentally generated chips. The stress patterns seem to be similar in all cases while on the other hand the actual values are somewhat different depending on the material model used in the simulations. The temperature distribution is also considered to be the same or similar in all cases. However, even though most parameters behave in a similar manner for all material models, residual stresses in the workpiece material differ quite significantly [32].

The change in the feed per tooth/tool edge radius ratio (f_{tooth}/t_r) also produces a change in the ratio of maximum cutting/thrust forces (F_C/F_T). As the chip thickness is decreased in the "down-cut milling" process, the cutting/thrust force ratio changes and is presented in Figs. 7, 8, 9, and 10. The transition from $F_C/F_T < 1$ (burr formation) to $F_C/F_T > 1$ (chip formation) defines a transition from burr-to-chip formation and is further characterized in Tables 2, 3, 4, 5, 6, and 7 using rations, F_C/F_T and f_{tooth}/t_r, for the simulations presented

Fig. 9 Cutting and thrust forces for **a** 10 μm tool edge radius and 5 μm feed rotating at 150,000 rpm spindle speed using a tungsten carbide cutting tool and **b** 4 μm tool edge radius and 4 μm feed rotating at 150,000 rpm spindle speed using a tungsten carbide cutting tool. The figures show the transition from burr-to-chip formation and the associated magnitude of force ratio
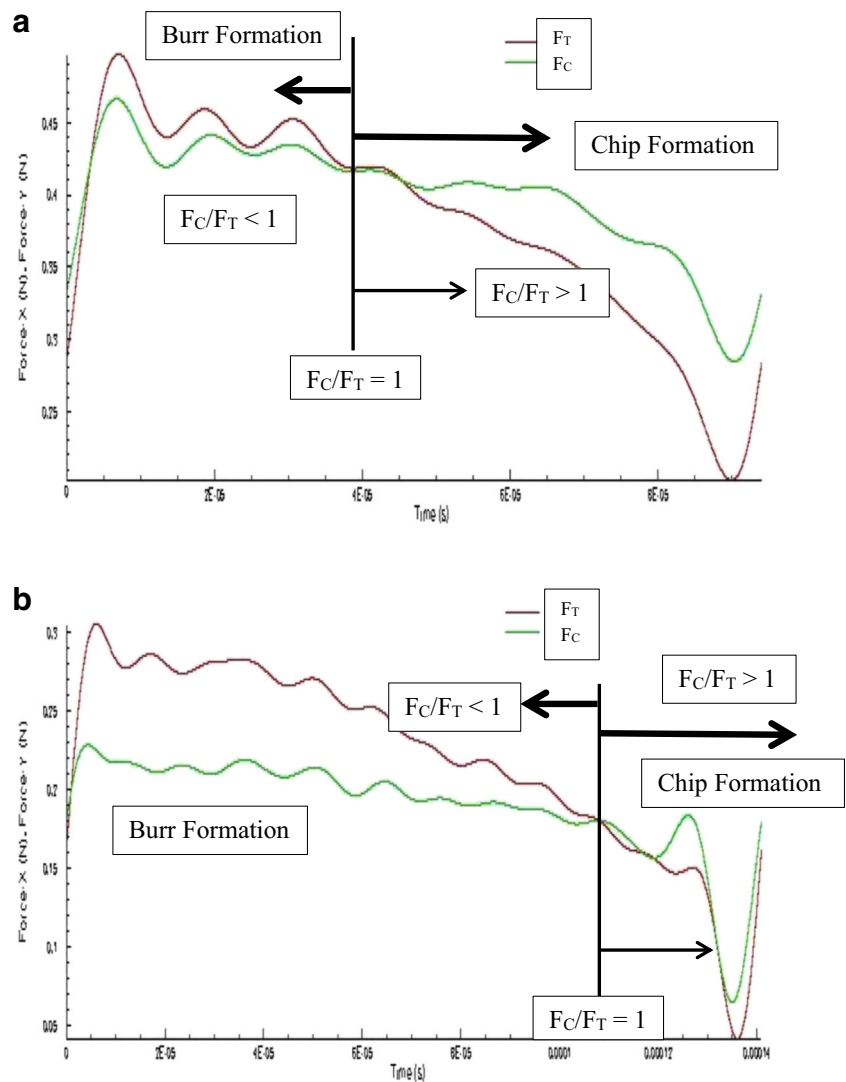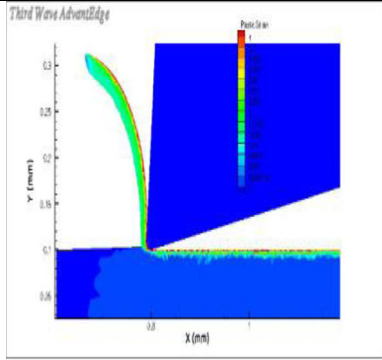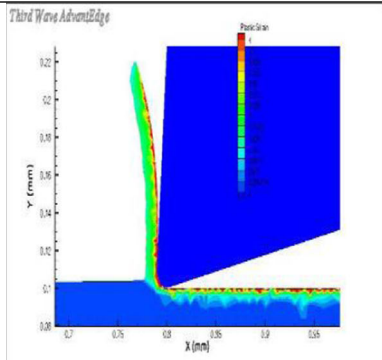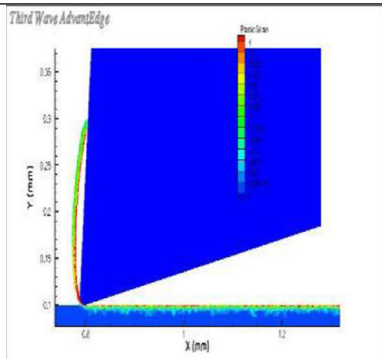

in this study. For all the simulations presented, the shear strain varies between 3.5 and 4 and the position of maximum shear strain moves from the chip to the surface of the workpiece as the tool edge radius decreases in magnitude. In terms of surface quality, it is advised that the feed per tooth should be as large as possible to minimize distortion of the surface of the workpiece by inducing shear strains into the chip rather than the surface of the machined workpiece.

5.2 Spindle speed and feed effects

It has been noticed that as the value for the rotational speed increases, the thrust force values show a direct dependence on rotational spindle speed yielding higher values [24]. The rise in the thrust force with the increase in rotational speed is attributed to the adherence of the chip to the cutting tool [25]. With the increase in temperature, adherence of the chip to the tool is actively promoted. The degree of adherence is considered to increase with the increase in speed due to the increase in

temperature, eventually resulting in the increase in thrust force. However, Robinson [26] showed that temperatures in micromachining commonly used engineering materials are very low, and when micromachining Ti6Al4V titanium alloy products, the maximum machining temperature stabilizes between 25 and 68 °C depending upon the machining parameters. Therefore, an absence of sustained heat flow at high temperatures allows one to predict that the chips generated during micromachining do not actually adhere to the cutting tool, and consequently, thrust forces do not change with an increase in the rotational speed of the cutting tool. The stability in computed magnitudes of forces with the consequent change in the rotational speed is shown in Figs. 11 and 12. For the tungsten carbide tools, the forces are relatively stable at the three magnitudes of cutting feeds. For diamond tools, the cutting forces are relatively stable, while the thrust force shows some level of stability that could be attributed to difference in hardness between using tungsten carbide and diamond as the tool material. This observation was also noted when micromilling AISI 1020 and 4140 steels [26] who

Fig. 10 Cutting and thrust forces for **a** 10 μm tool edge radius and 5 μm feed rotating at 200,000 rpm spindle speed using a tungsten carbide cutting tool and **b** 4 μm tool edge radius and 4 μm feed rotating at 200,000 rpm spindle speed using a tungsten carbide cutting tool. The figures show the transition from burr-to-chip formation and the associated magnitude of force ratio
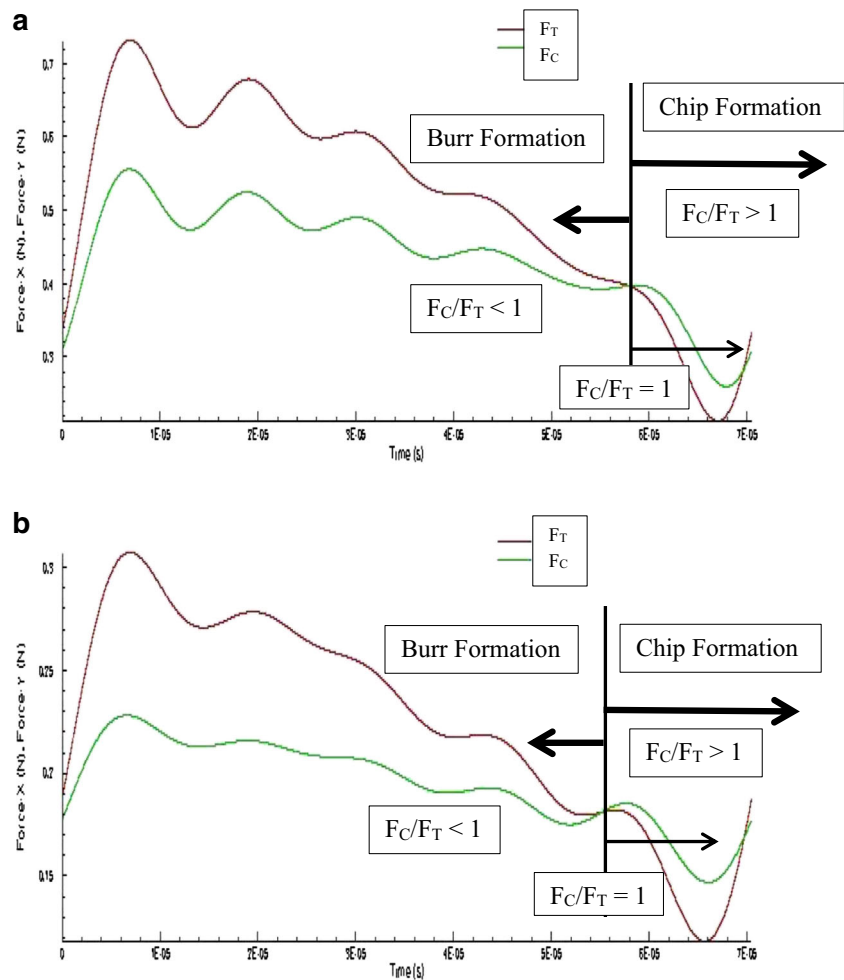
validated the use of FEA for analyzing forces and effects on chip formation and shape.

The influence of the feed per tooth when micromachining Ti6Al4V titanium alloy is significant in terms of cutting and thrust forces. The point at which the forces are equal is used to define the stability of the process and the recommended parameters in terms of feed per tooth, tool diameter, and spindle speed. It is shown in Figs. 13 and 14 that cutting and thrust forces increase with increases in the feed/tooth. The transition points define three stages of machining: (A) burr formation, (B) mixed mode region of cutting, plowing and sliding, and (C) chip formation. There is a strong similarity when the results are compared with the results demonstrated by Kim and Kim [27] who had based their research on the differentiation of micro and macrocutting processes. Their research shows that the increasing force with the depth of cut is accounted for by three components of factors, the rake face, the contact point of the workpiece, and the tool's clearance face, which can cause elastic spring back of the workpiece material and tool and the rounding effect of the edge of the tool. The studies conducted in this paper appear to validate their work and that of Robinson's [26, 27].

5.3 Temperatures, distribution, and changes in heating rate

Temperature is considered to be another one of the commonly investigated issues using FEA in the process of machining. Usui et al. [33] investigated the tool edge temperature and its effect on the wear characteristics in machining with ceramic tools. The influence of the cutting speed on the temperature generated in the tool has been investigated showing that there is a significant increase in the tool temperature with a higher value registered for the rake compared to flank face of the tool [34]. The fact that the tool temperature increases with the increase in cutting speed was confirmed [33], and it has been shown that the temperatures are close to the melting temperature of the workpiece material. Kim et al. used finite element modeling to determine temperature and stress distributions in micromachining [35]. The researchers chose oxygen-free copper as the workpiece material, while the tool was a diamond cutter. It was presented that the highest temperature occurred within the shear plane as it reaches 562 °C even though the depth of cut is only 2 μm. They determined that if the effect of the temperature is ignored, the values obtained for the flow

Table 2 Effect of the feed per tooth/tool edge radius ratio (f_{tooth}/t_r) on chip and non-chip (burr) formation with the associated force condition (tungsten carbide cutting tool). Simulation conditions: 10 μm tool edge radius, 10, 5, and 3.125 μm feed/tooth, and 100,000 rpm spindle speed using a tungsten carbide tool
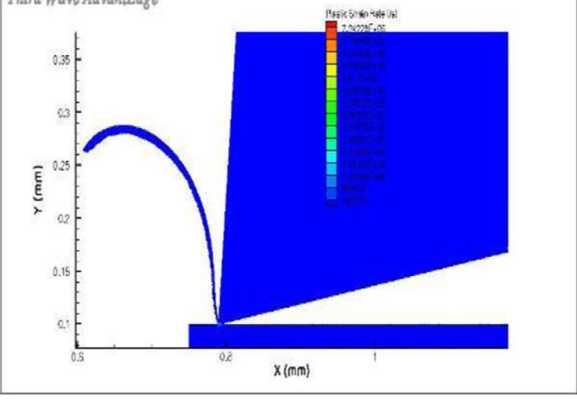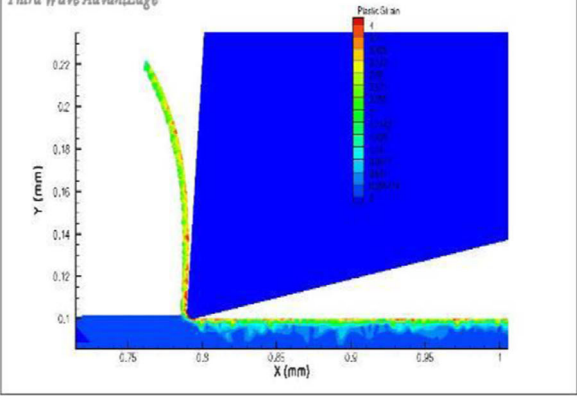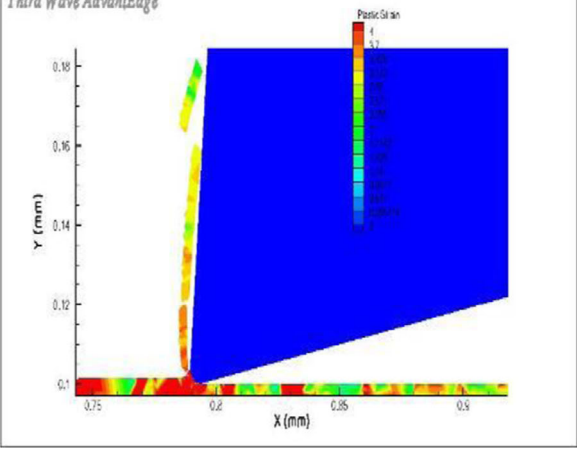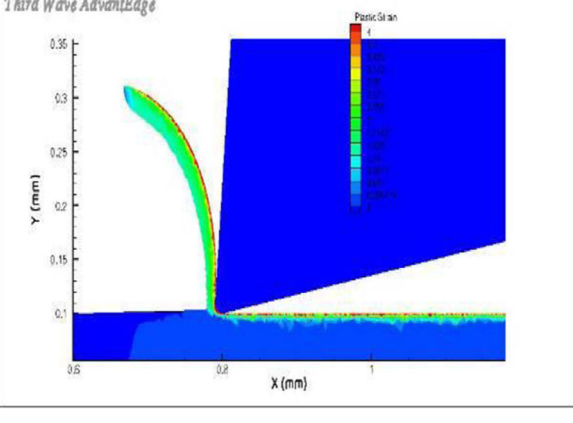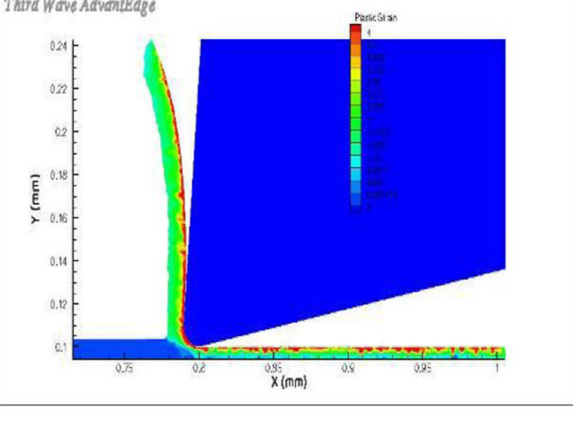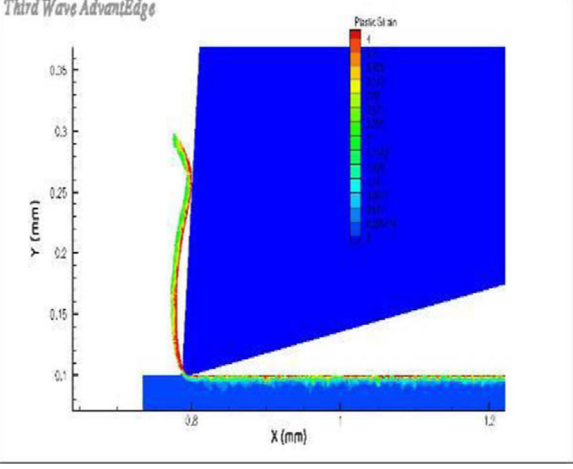
Simulation condition	Chip formation simulation (plastic strain)	Feed per tooth /tool edge ratio, (f_{tooth}/t_r)	Cutting force condition, F_C and F_T
10μm tool edge radius, 10 μm feed/tooth and 100,000 rpm spindle speed using a tungsten carbide tool.		1	$F_C > F_T$
10 μm tool edge radius, 5 μm feed/tooth and 100,000 rpm spindle speed using a tungsten carbide tool.		0.5	$F_C = F_T$
10 μm tool edge radius, 3.125 μm feed/tooth and 100,000 rpm spindle speed using a tungsten carbide tool.		~0.3	$F_C < F_T$

stress are doubled when compared to the experimental one resulting in forces considerably higher than those measured. Cao et al. [36] concluded in their research findings that the maximum cutting temperature depends greatly on the tool edge radius and it increases with the increase in tool edge radius. It has also been noticed that the effect of the radius is not only on the magnitude of the temperature generated during machining but on the temperature field distribution and direction as well. In the present work, when the change in heating rate at the point where $F_C = F_T$ is analyzed (mixed mode cutting/sliding), there is a transition of forces from $F_C/F_T < 1$ to $F_C/F_T > 1$. When $F_C/F_T < 1$, burr formation is

Table 3 Effect of the feed per tooth/tool edge radius ratio (f_{tooth}/t_r) on chip and non-chip (burr) formation with the associated force condition (tungsten carbide cutting tool). Simulation conditions: 4 μm tool edge radius, 4, 2, and 1.25 μm feed/tooth, and 100,000 rpm spindle speed using a tungsten carbide tool
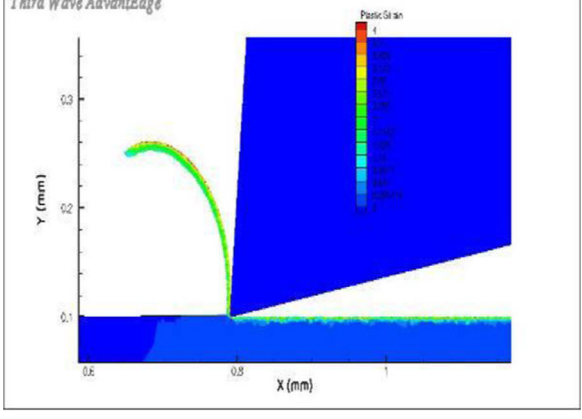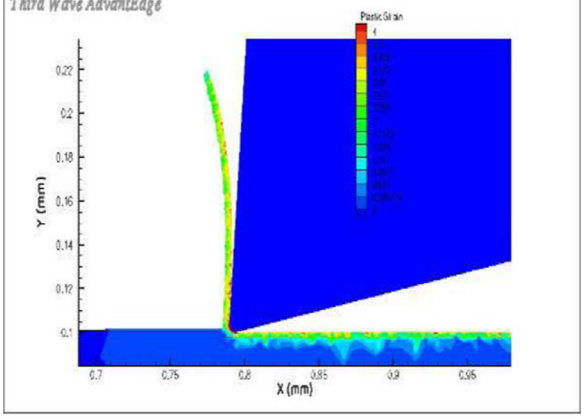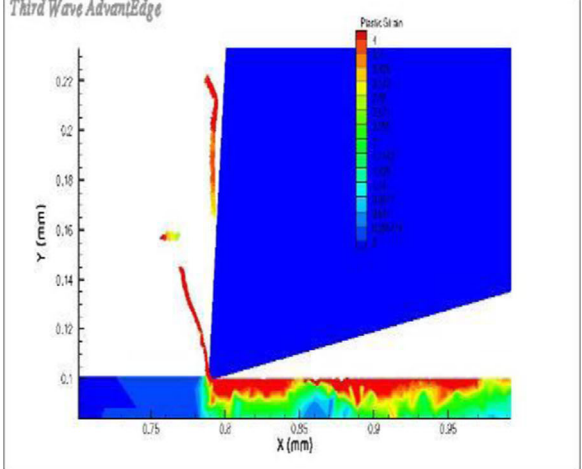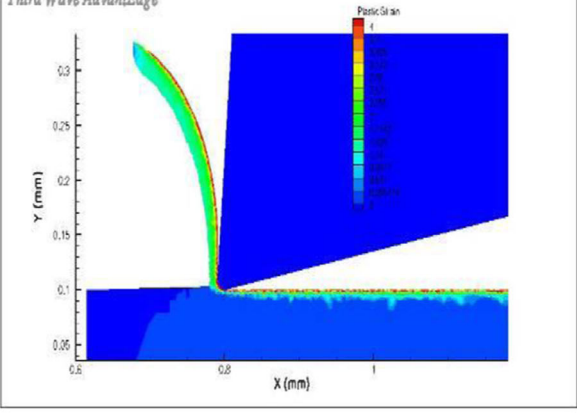
Simulation condition	Chip formation simulation (plastic strain)	Feed per tooth /tool edge ratio, (f_{tooth}/t_r)	Cutting force condition, F_C and F_T
4μm tool edge radius, 4 μm feed/tooth and 100,000 rpm spindle speed using a tungsten carbide tool.		1	$F_C > F_T$
4 μm tool edge radius, 2 μm feed/tooth and 100,000 rpm spindle speed using a tungsten carbide tool.		0.5	$F_C = F_T$
4 μm tool edge radius, 1.25 μm feed/tooth and 100,000 rpm spindle speed using a tungsten carbide tool.		~0.3	$F_C < F_T$

Table 4 Effect of the feed per tooth/tool edge radius ratio (f_{tooth}/t_r) on chip and non-chip (burr) formation with the associated force condition (tungsten carbide cutting tool). Simulation conditions: 10 µm tool edge radius, 10, 5, and 3.125 µm feed/tooth, and 150,000 rpm spindle speed using a tungsten carbide tool
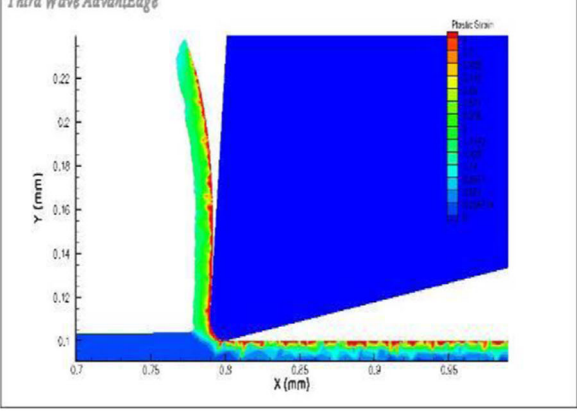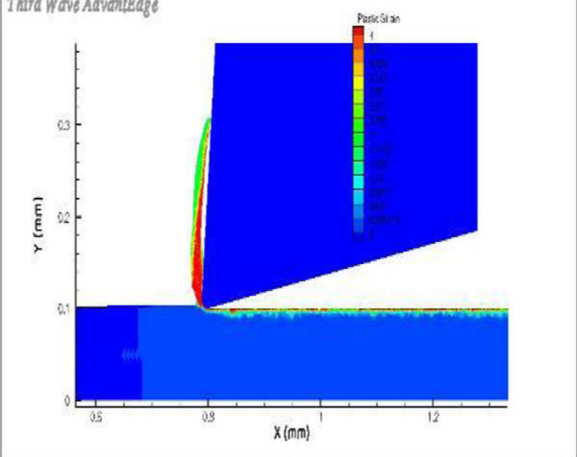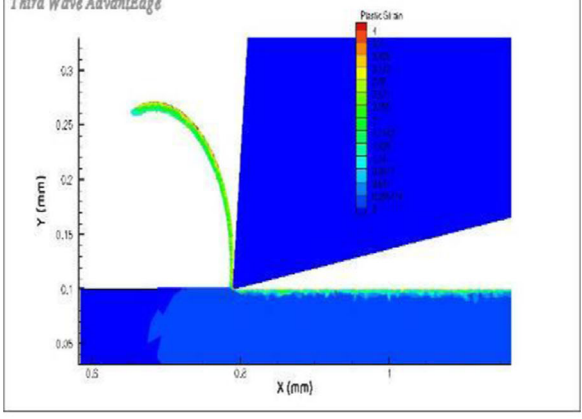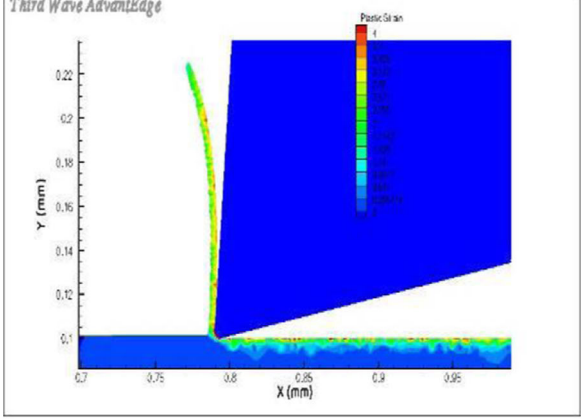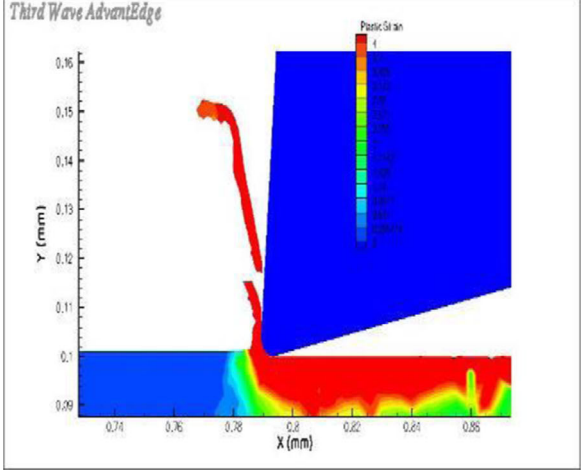
Simulation condition	Chip formation simulation (plastic strain)	Feed per tooth /tool edge ratio, (f_{tooth}/t_r)	Cutting force condition, F_C and F_T
10µm tool edge radius, 10 µm feed/tooth and 150,000 rpm spindle speed using a tungsten carbide tool.		1	$F_C > F_T$
10 µm tool edge radius, 5 µm feed/tooth and 150,000 rpm spindle speed using a tungsten carbide tool.		0.5	$F_C = F_T$
10 µm tool edge radius, 3.125 µm feed/tooth and 150,000 rpm spindle speed using a tungsten carbide tool.		~0.3	$F_C < F_T$

Table 5 Effect of the feed per tooth/tool edge radius ratio (f_{tooth}/t_r) on chip and non-chip (burr) formation with the associated force condition (tungsten carbide cutting tool). Simulation conditions: 4 μm tool edge radius, 4, 2, 1.25 μm feed/tooth and 150,000 rpm spindle speed using a tungsten carbide tool

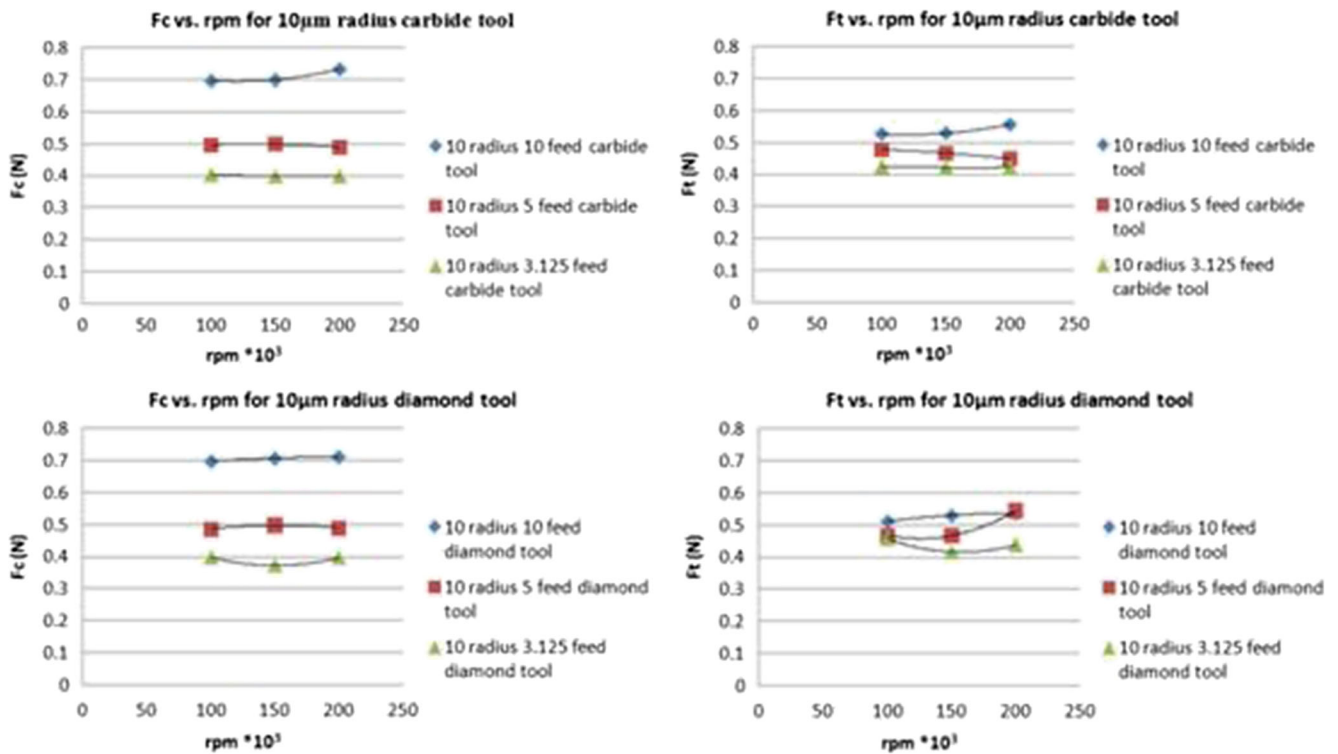| Simulation condition	Chip formation simulation (plastic strain)	Feed per tooth /tool edge ratio, (f_{tooth}/t_r)	Cutting force condition, F_C and F_T
4 μm tool edge radius, 4 μm feed/tooth and 150,000 rpm spindle speed using a tungsten carbide tool.		1	$F_C > F_T$
4 μm tool edge radius, 2 μm feed/tooth and 150,000 rpm spindle speed using a tungsten carbide tool.		0.5	$F_C = F_T$
4 μm tool edge radius, 1.25 μm feed/tooth and 150,000 rpm spindle speed using a tungsten carbide tool.		~0.3	$F_C < F_T$

Table 6 Effect of the feed per tooth/tool edge radius ratio (f_{tooth}/t_r) on chip and non-chip (burr) formation with the associated force condition (tungsten carbide cutting tool). Simulation conditions: 10 μm tool edge radius, 10, 5, and 3.125 μm feed/tooth, and 200,000 rpm spindle speed using a tungsten carbide tool

Simulation condition	Chip formation simulation (plastic strain)	Feed per tooth /tool edge ratio, (f_{tooth}/t_r)	Cutting force condition, F_C and F_T
10μm tool edge radius, 10 μm feed/tooth and 200,000 rpm spindle speed using a tungsten carbide tool.		1	$F_C > F_T$
10 μm tool edge radius, 5 μm feed/tooth and 200,000 rpm spindle speed using a tungsten carbide tool.		0.5	$F_C = F_T$
10 μm tool edge radius, 3.125 μm feed/tooth and 200,000 rpm spindle speed using a tungsten carbide tool.		~0.3	$F_C < F_T$

Table 7 Effect of the feed per tooth/tool edge radius ratio (f_{tooth}/t_r) on chip and non-chip (burr) formation with the associated force condition (tungsten carbide cutting tool). Simulation conditions: 4 μm tool edge radius, 4, 2, and 1.25 μm feed/tooth, and 200,000 rpm spindle speed using a tungsten carbide tool

Simulation condition	Chip formation simulation (plastic strain)	Feed per tooth /tool edge ratio, (f_{tooth}/t_r)	Cutting force condition, F_C and F_T
4μm tool edge radius, 4 μm feed/tooth and 200,000 rpm spindle speed using a tungsten carbide tool.		1	$F_C > F_T$
4 μm tool edge radius, 2 μm feed/tooth and 200,000 rpm spindle speed using a tungsten carbide tool.		0.5	$F_C = F_T$
4 μm tool edge radius, 1.25 μm feed/tooth and 200,000 rpm spindle speed using a tungsten carbide tool.		~0.3	$F_C < F_T$

Fig. 11 Computed cutting and thrust forces as a function of spindle speed for a 10-μm edge radius cutting tool (tungsten carbide and diamond cutting tool materials). Cutting feeds are **a** 10 μm feed/tooth, **b** 5 μm feed/tooth, and **c** 3.125 μm feed/tooth

predominant and when $F_C/F_T > 1$, the chip formation is prevalent. It can be seen from Figs. 15, 16, 17, 18, 19, 20, 21, 22, 23, 24, 25, and 26 that there is a drastic difference in the shape and position of the thermal field. The heating rate field
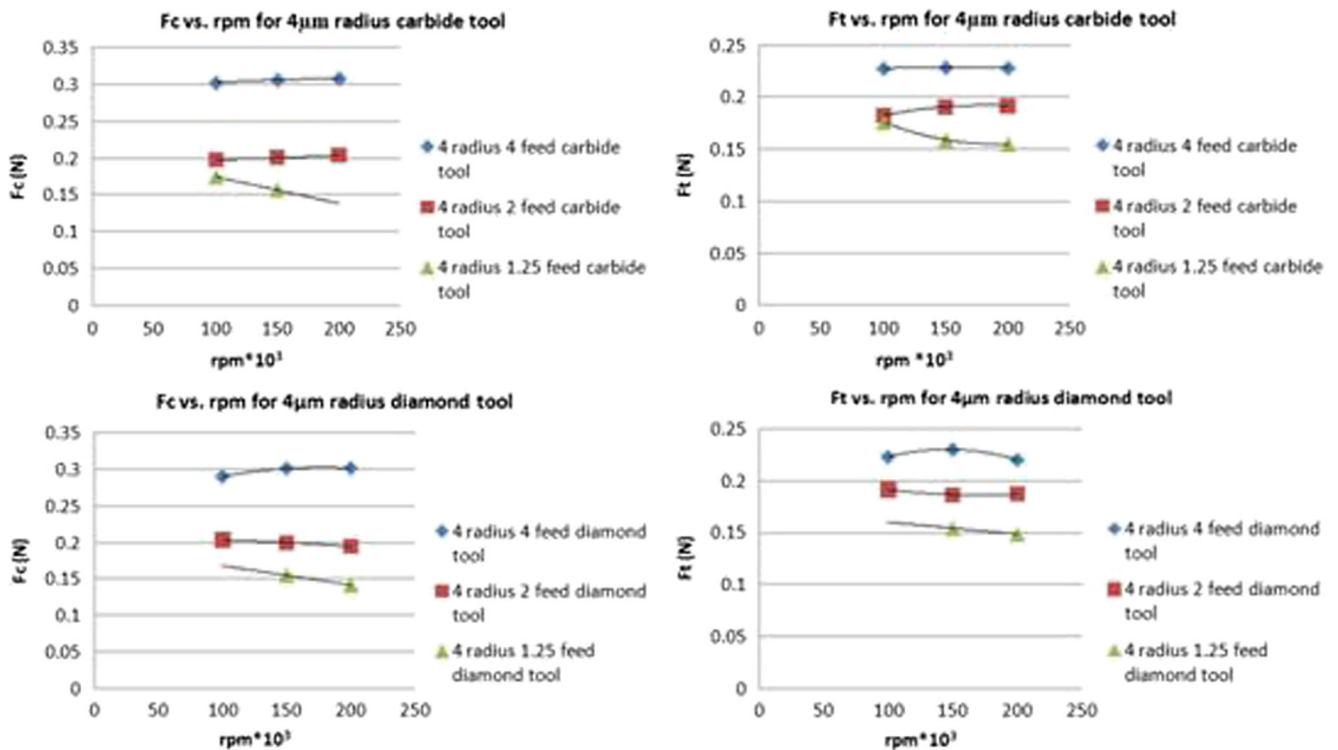
Fig. 12 Computed cutting and thrust forces as a function of spindle speed for a 4-μm edge radius cutting tool (tungsten carbide and diamond cutting tool materials). Cutting feeds are **a** 4 μm feed/tooth, **b** 2 μm feed/tooth, and **c** 1.25 μm feed/tooth
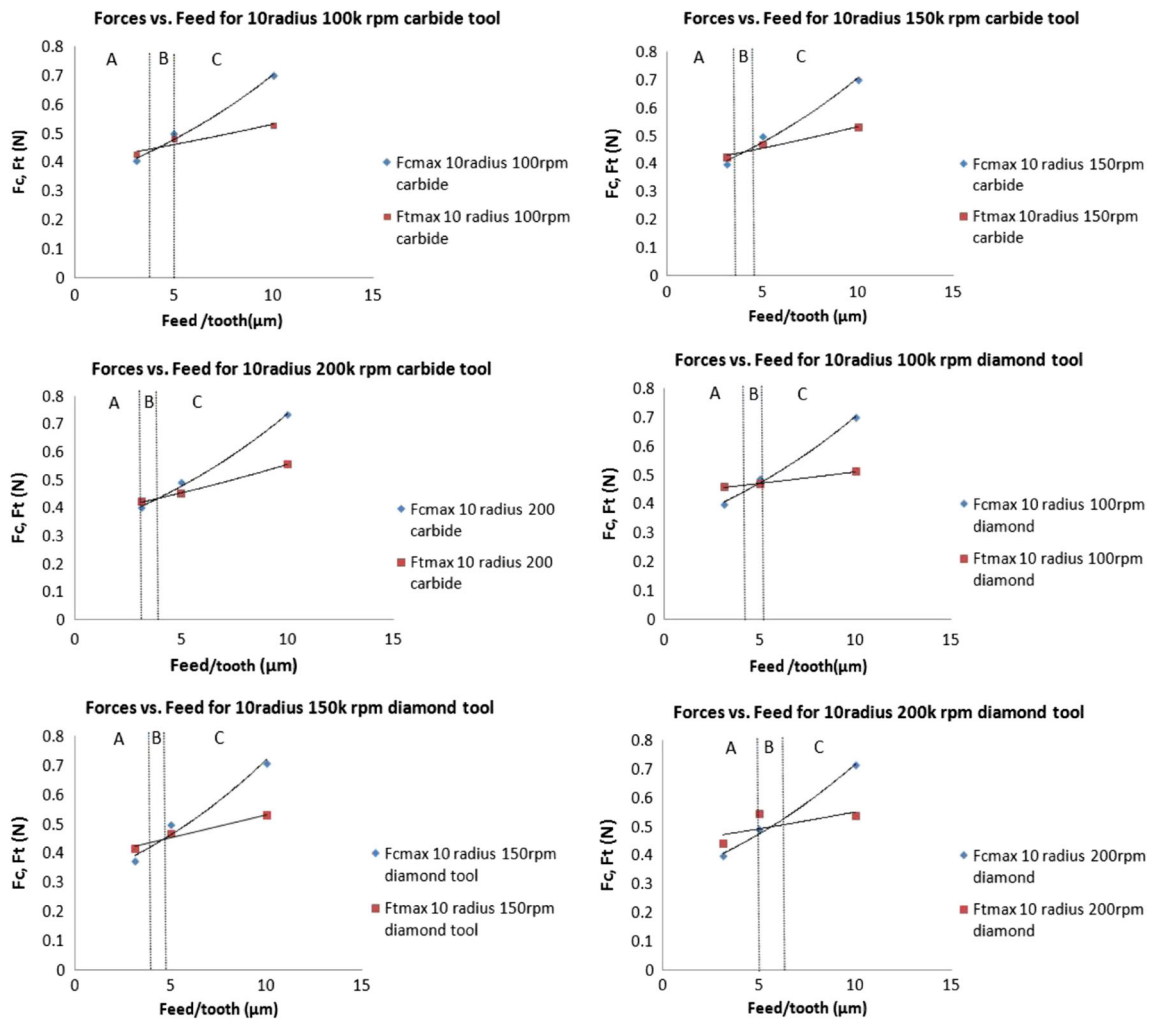
Fig. 13 Force versus feed/tooth for a 10-μm tool edge radius cutting tool at various spindle speeds and cutting tool material. *A* denotes $F_C/F_T < 1$ (burr formation), *B* denotes $F_C/F_T = 1$, and *C* denotes $F_C/F_T > 1$ (chip formation)

changes direction when there is a change from burr formation to chip formation. Before the transition, i.e., when stable machining and chip formation is present, the heating rate field is located in the chip root showing that the heat will dissipate into the chip rather than into the workpiece. The heat is then taken away by the chips from the tool and workpiece. It can be seen that the highest heating rate occurs at the chip root and is concentrated in one area with no distinctive dissipation path identified. Upon crossing into the region of burr formation, the heating rate field can be seen to move away from the free surface of the chip towards the tool and under the tool into the workpiece. Rather than going into the burr, the heat is partitioned into the workpiece. The partitioned heat could be considered responsible for the re-welding of the cracks in the burrs as it is pushed out of the tool–work material contact zone. It can be seen that the highest heating rate covers a larger area below the tool as well as below the chip root into the bulk of the work material. This change in the position of the heat rate field is expected to occur and is in accordance with the phenomena associated with the burr-to-chip transition [26]. The

phenomenon appears to be in accordance with Cao [36] and other researchers [37–38]. In terms of surface quality, it is advised that the chip formation is promoted in order to partition the heat into the chip rather than into the workpiece material. For chip formation conditions to occur, the ration F_C/F_T should be greater than unity ($F_C/F_T > 1$) and the ration of feed per tooth to tool edge radius should be approximately unity, i.e., $f_{tooth}/t_r \sim 1$.

6 Conclusions

When manufacturing microscale products, it is necessary to determine the correct machining parameters in order to achieve the efficient removal of material and associated levels of quality one expects from a microscale device. It has been determined that when micromachining Ti6Al4V titanium, that when the magnitude of the cutting force is higher than the thrust force ($F_C/F_T > 1$), chip formation occurs and that chip curl is caused by the bending moment which acts at the root of the chip. When
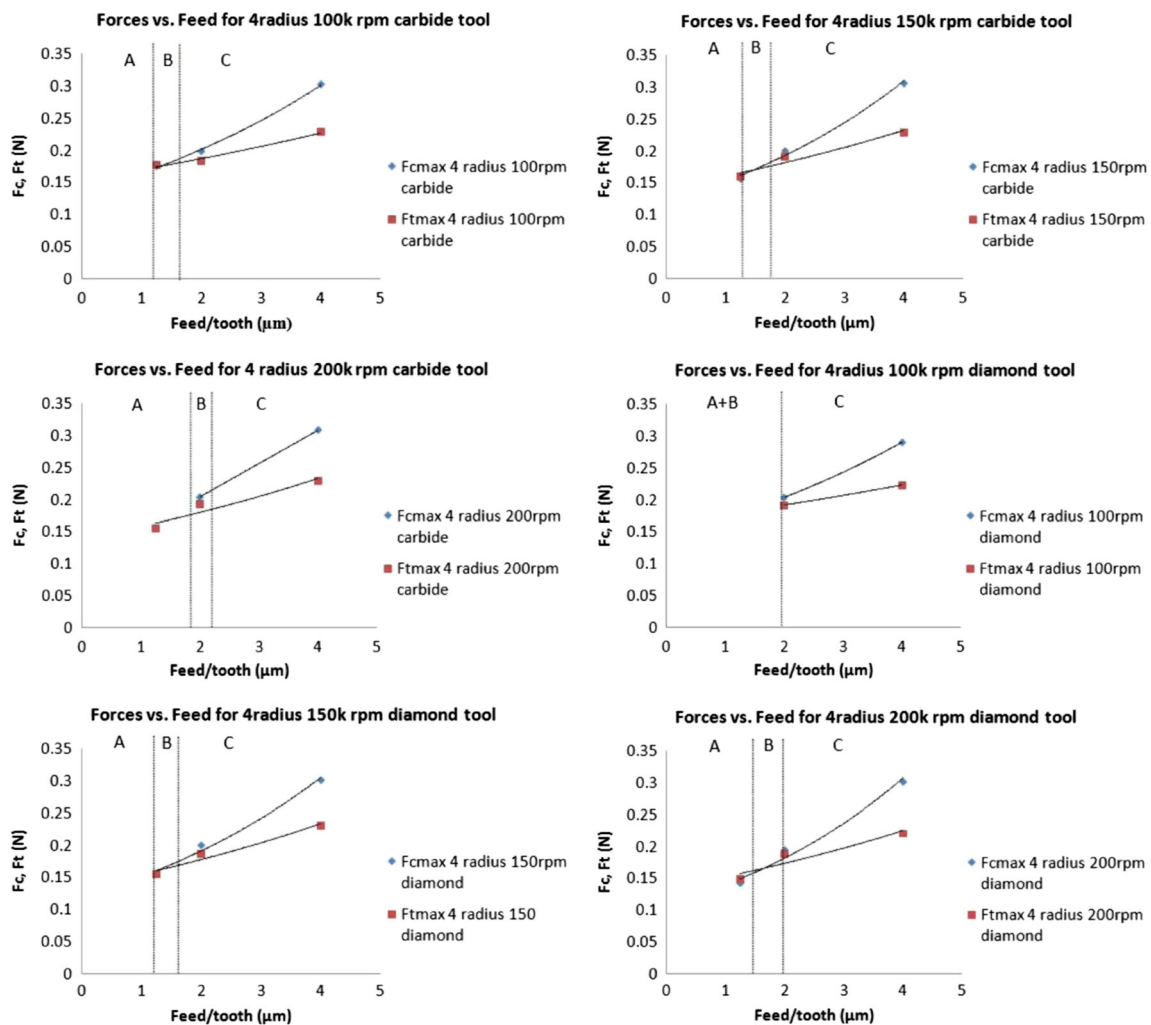
Fig. 14 Force versus feed/tooth for a 4-µm tool edge radius cutting tool at various spindle speeds and cutting tool material. *A* denotes $F_C/F_T < 1$ (burr formation), *B* denotes $F_C/F_T = 1$, and *C* denotes $F_C/F_T > 1$ (chip formation)

the cutting and thrust forces are equal in magnitude ($F_C = F_T$), the bending moment diminishes, leaving a vertical chip to form where burr and chip formation exists simultaneously. When the cutting force is lower in magnitude than the thrust force ($F_C/F_T < 1$), chip formation ceases and burr formation is promoted. Work material detached by the cutting edge is bent towards the tool, showing an opposite bending moment when compared with the case of chip formation. Furthermore, the heating rate is seen to change drastically when the aforementioned transition occurs. During the chip formation process, the heating rate field is situated close to the root of the chip moving directly into the chip and away from the workpiece surface. As the transition to burr formation occurs, the heating rate field moves into direction of the workpiece and under the tool as the chip-to-burr transition takes place.

The transition from the chip-to-burr formation can also be observed when the ratio of feed per tooth to tool edge radius is analyzed. When the ratio of feed per tooth to tool edge radius is approximately unity ($f_{tooth}/t_r \sim 1$), the process forms chips.

When the ratio it decreased equal to 0.5 ($f_{tooth}/t_r = 0.5$), chip formation and burr formation exist simultaneously. However, when the ratio approaches an approximate value of 0.3 ($f_{tooth}/t_r \sim 0.3$), burr formation is dominant. This information is considered extremely important when determining the minimum size of the features produced by the micromilling process. Also, as the tool edge radius decreases in magnitude, the position of maximum shear strain moves from the chip to the surface of the workpiece material.

Finally, it has been determined that the rotational speed has a different influence at the microscale than it does at the macroscale. Chip formation is defined by the adherence of the chip to the cutting tool due to the high temperatures generated in the macromachining of the Ti6Al4V titanium alloy (thermal effects are clearly very important at the macroscale). The lack of chip adherence and low temperatures generated at the tool–workpiece contact zone at the microscale (~25 to 68 °C) implies that a different mechanism of chip formation is operating
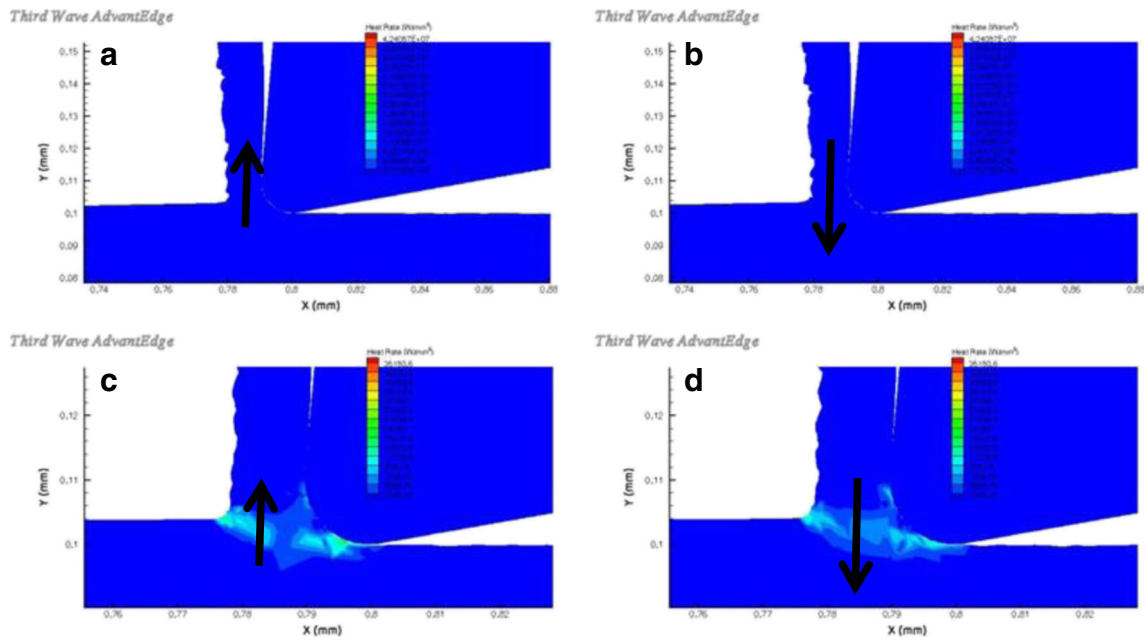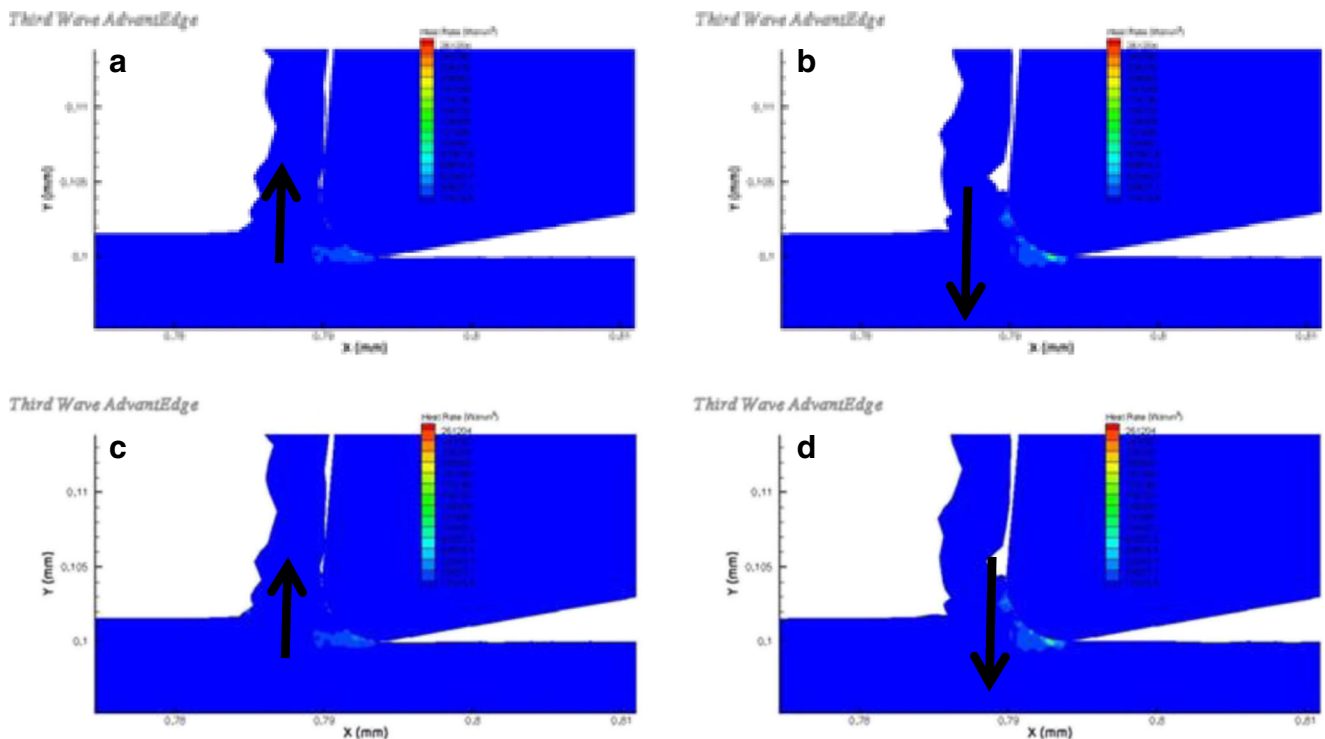
Fig. 15 The change in the direction of the heating rate for a 10-μm radius cutting tool operating at 100,000 rpm with a tungsten carbide cutting tool: **a** 10 μm feed/tooth when $F_C/F_T > 1$ (chip formation), **b** 10 μm feed/tooth when $F_C/F_T < 1$ (burr formation), **c** 5 μm feed/tooth when $F_C/F_T > 1$ (chip formation), and **d** 5 μm feed/tooth when $F_C/F_T < 1$ (burr formation). The *arrows* show the direction of movement of the thermal field

at the microscale and that the mechanism is clearly heavily dependent on kinematic effects rather than thermal effects, as observed by other research works on FEA of micromachining processes [26, 28–38].

Further computational and experimental work is planned to extend the range of alloys, cutting tools, and operational parameters used in the current work. The authors hope to experimentally validate the conclusions drawn from this study.

Fig. 16 The change in the direction of the heating rate for a 4-μm radius cutting tool operating at 100,000 rpm with a tungsten carbide cutting tool: **a** 4 μm feed/tooth when $F_C/F_T > 1$ (chip formation), **b** 4 μm feed/tooth when $F_C/F_T < 1$ (burr formation), **c** 2 μm feed/tooth when $F_C/F_T > 1$ (chip formation), and **d** 2 μm feed/tooth when $F_C/F_T < 1$ (burr formation). The *arrows* show the direction of movement of the thermal field
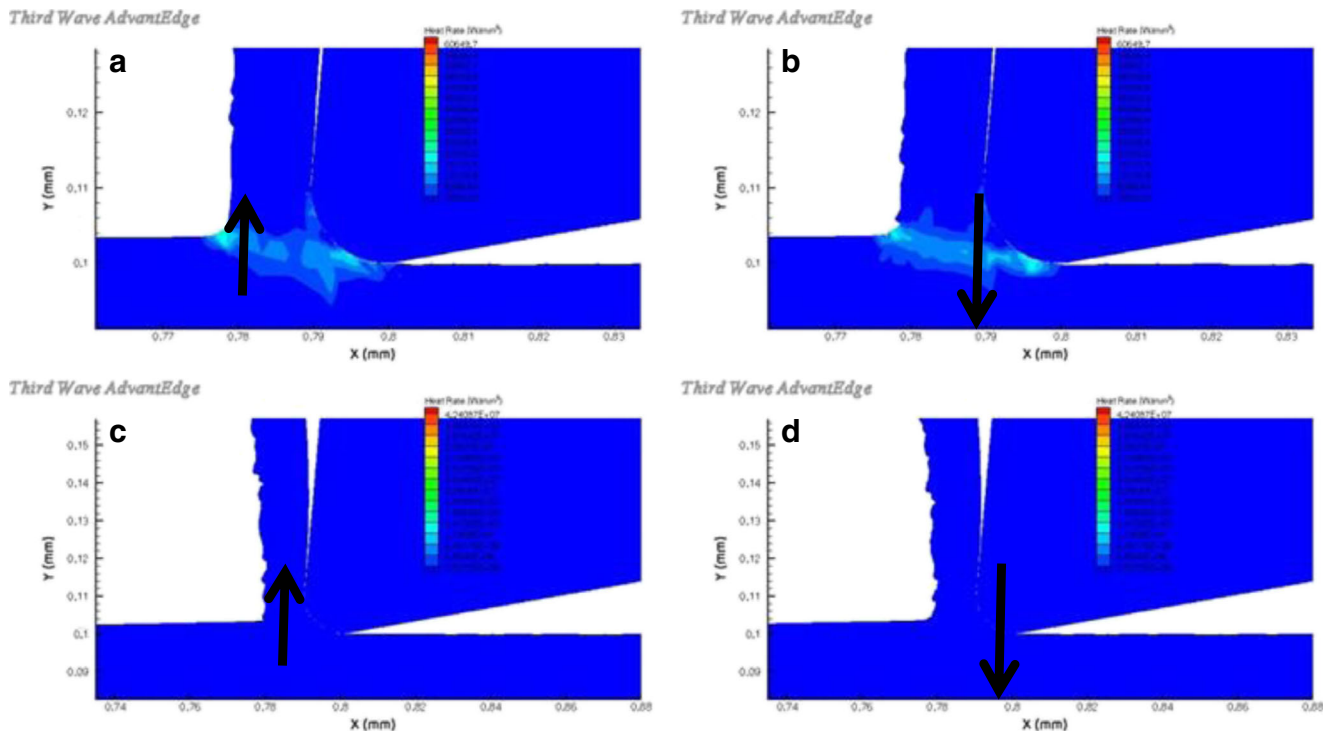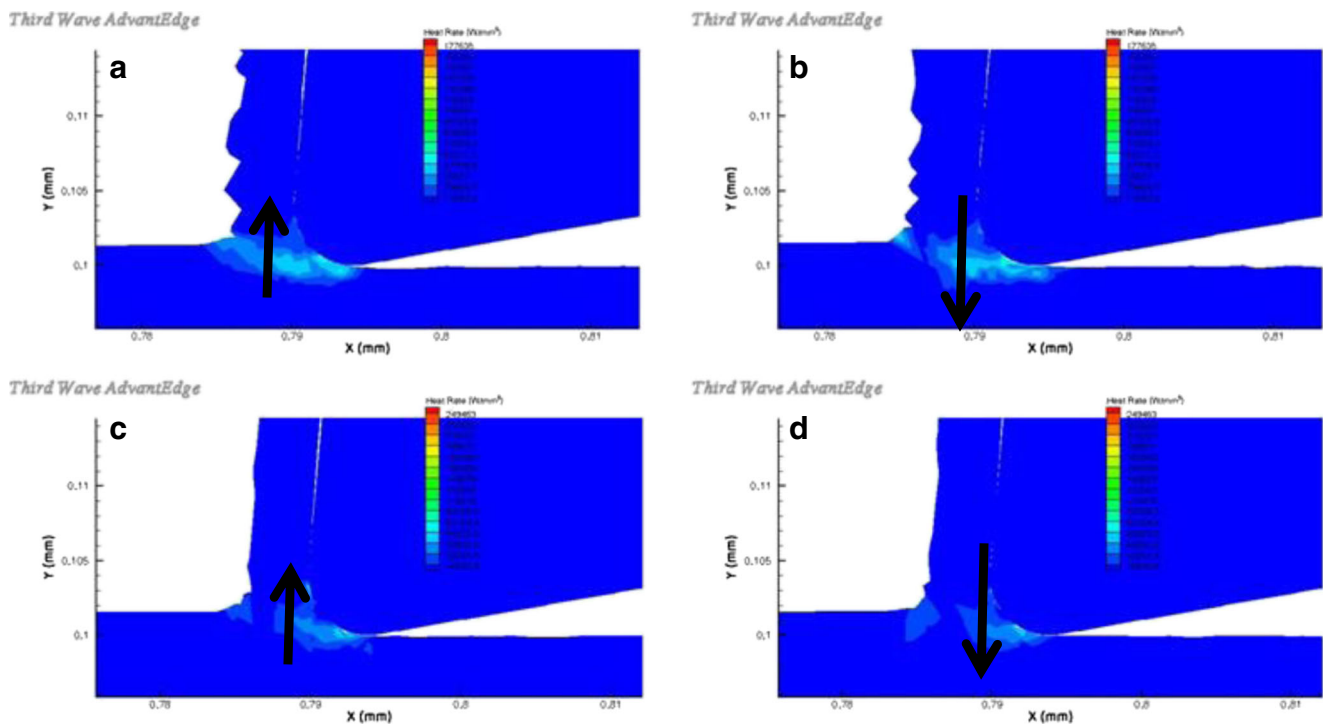
Fig. 17 The change in the direction of the heating rate for a 10-μm radius cutting tool operating at 150,000 rpm with a tungsten carbide cutting tool: **a** 10 μm feed/tooth when $F_C/F_T > 1$ (chip formation), **b** 10 μm feed/tooth when $F_C/F_T < 1$ (burr formation), **c** 5 μm feed/tooth when $F_C/F_T > 1$ (chip formation), and **d** 5 μm feed/tooth when $F_C/F_T < 1$ (burr formation). The *arrows* show the direction of movement of the thermal field
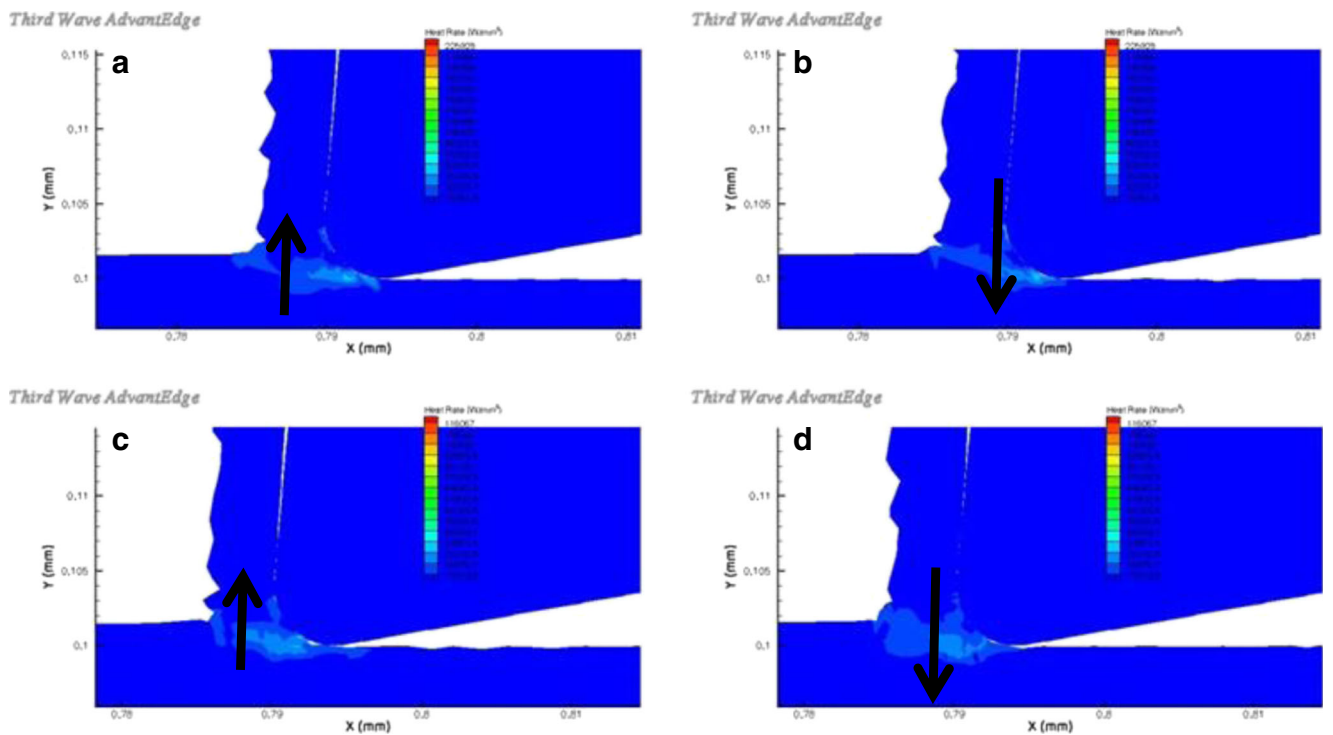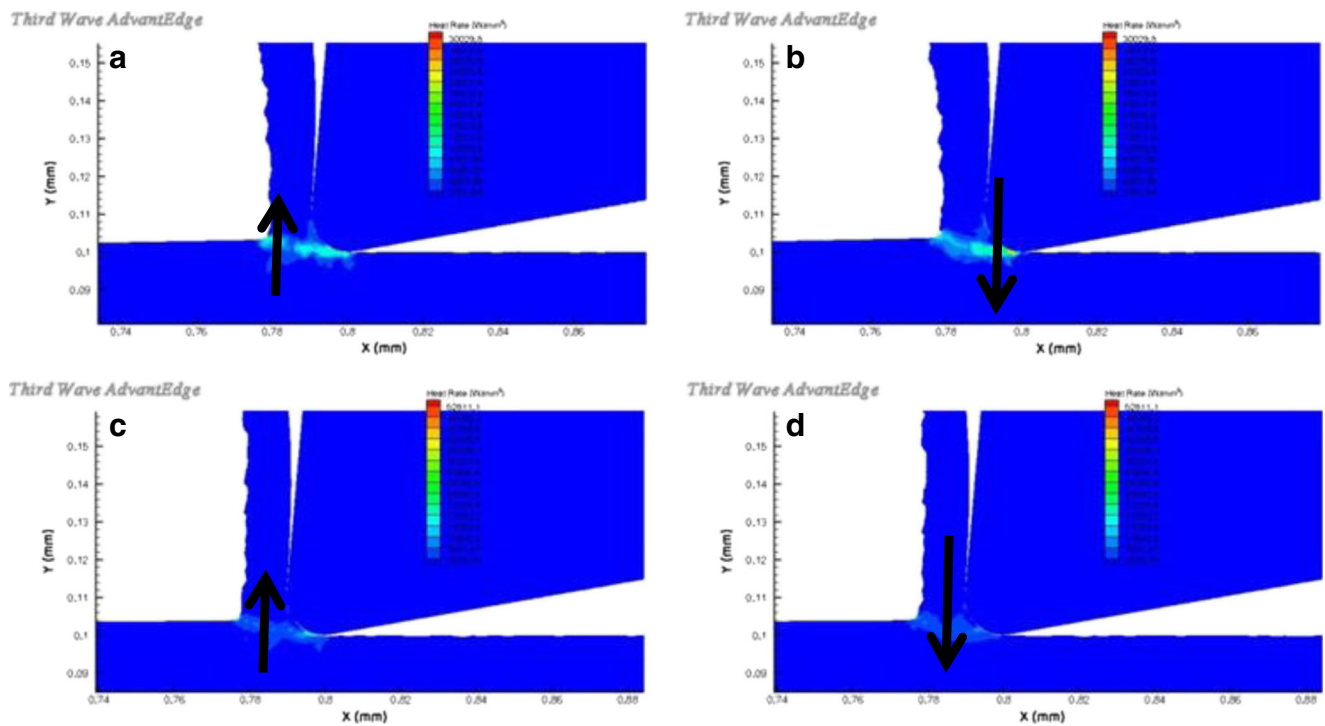

Fig. 18 The change in the direction of the heating rate for a 4-μm radius cutting tool operating at 150,000 rpm with a tungsten carbide cutting tool: **a** 4 μm feed/tooth when $F_C/F_T > 1$ (chip formation), **b** 4 μm feed/tooth when $F_C/F_T < 1$ (burr formation), **c** 2 μm feed/tooth when $F_C/F_T > 1$ (chip formation), 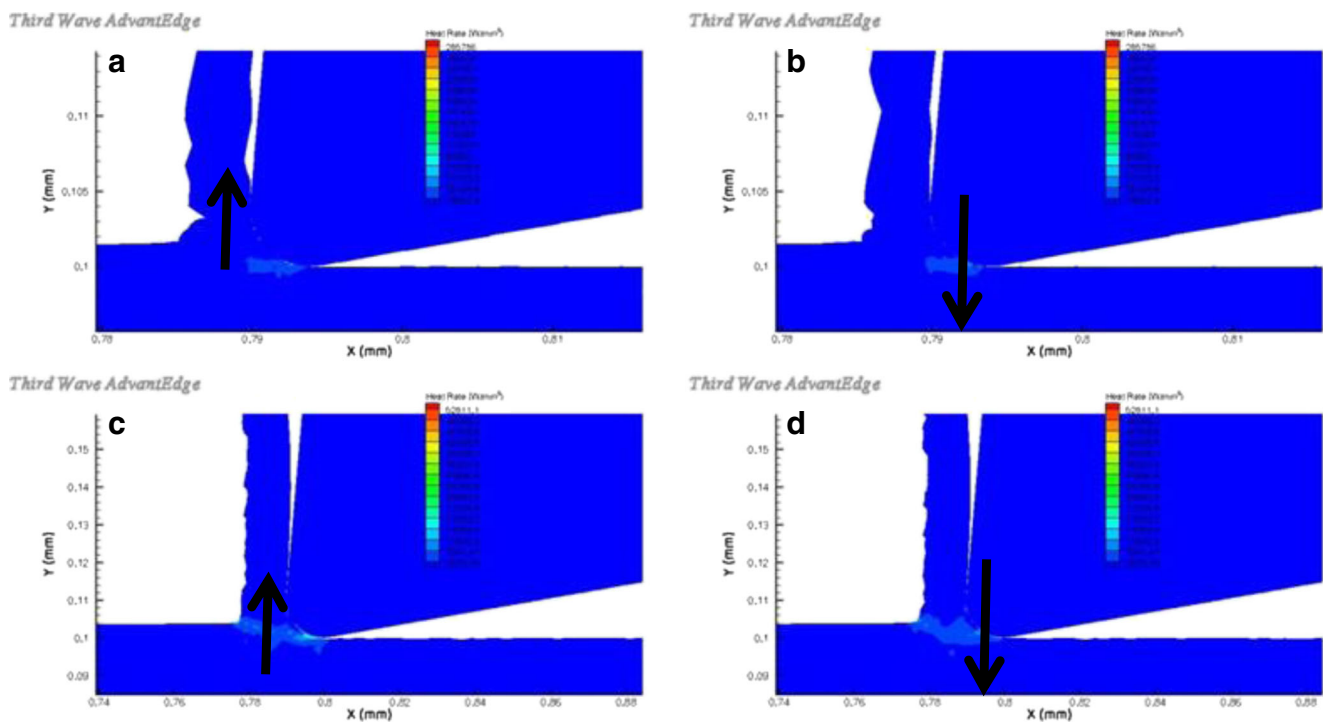and **d** 2 μm feed/tooth when $F_C/F_T < 1$ (burr formation). The *arrows* show the direction of movement of the thermal field
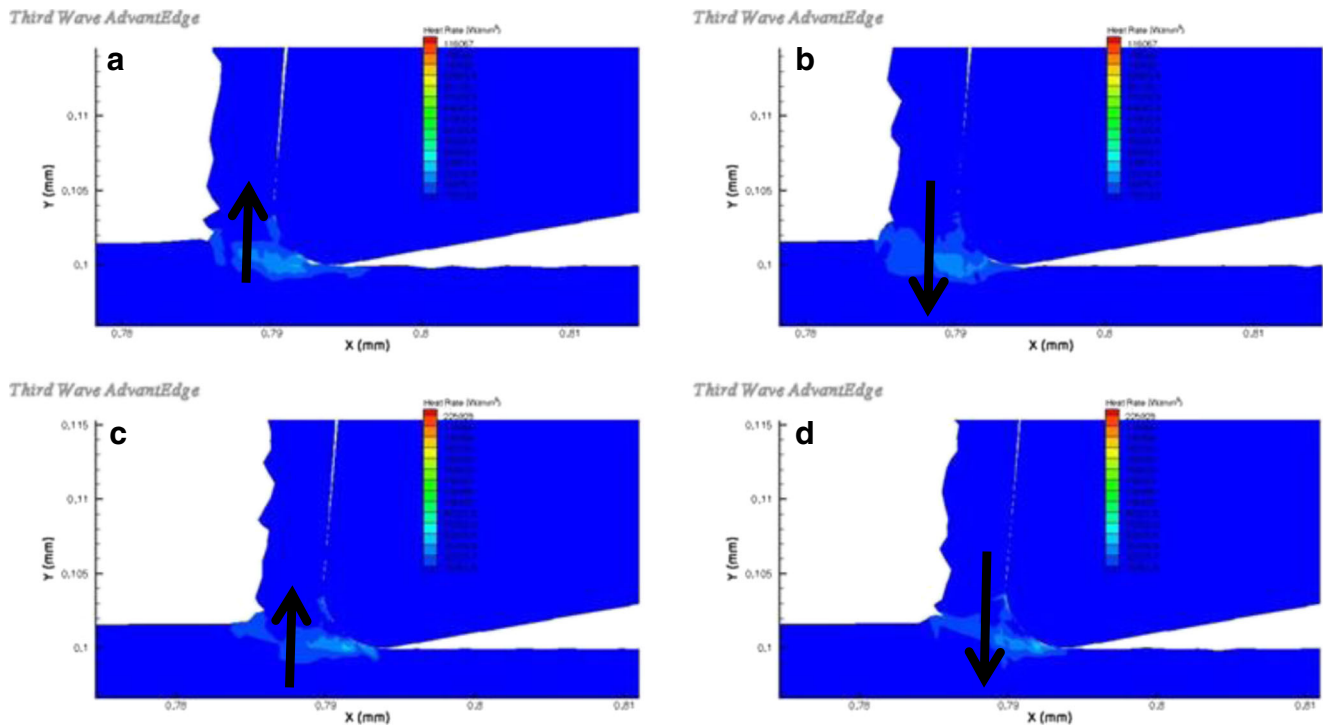
Fig. 19 The change in the direction of the heating rate for a 10-μm radius cutting tool operating at 200,000 rpm with a tungsten carbide cutting tool: **a** 10 μm feed/tooth when $F_C/F_T > 1$ (chip formation), **b** 10 μm feed/tooth when $F_C/F_T < 1$ (burr formation), **c** 5 μm feed/tooth when $F_C/F_T > 1$ (chip formation), and **d** 5 μm feed/tooth when $F_C/F_T < 1$ (burr formation). The arrows *show* the direction of movement of the thermal field

Fig. 20 The change in the direction of the heating rate for a 4-μm radius cutting tool operating at 200,000 rpm with a tungsten carbide cutting tool: **a** 4 μm feed/tooth when $F_C/F_T > 1$ (chip formation), **b** 4 μm feed/tooth when $F_C/F_T < 1$ (burr formation), **c** 2 μm feed/tooth when $F_C/F_T > 1$ (chip formation), and **d** 2 μm feed/tooth when $F_C/F_T < 1$ (burr formation). The *arrows* show the direction of movement of the thermal field
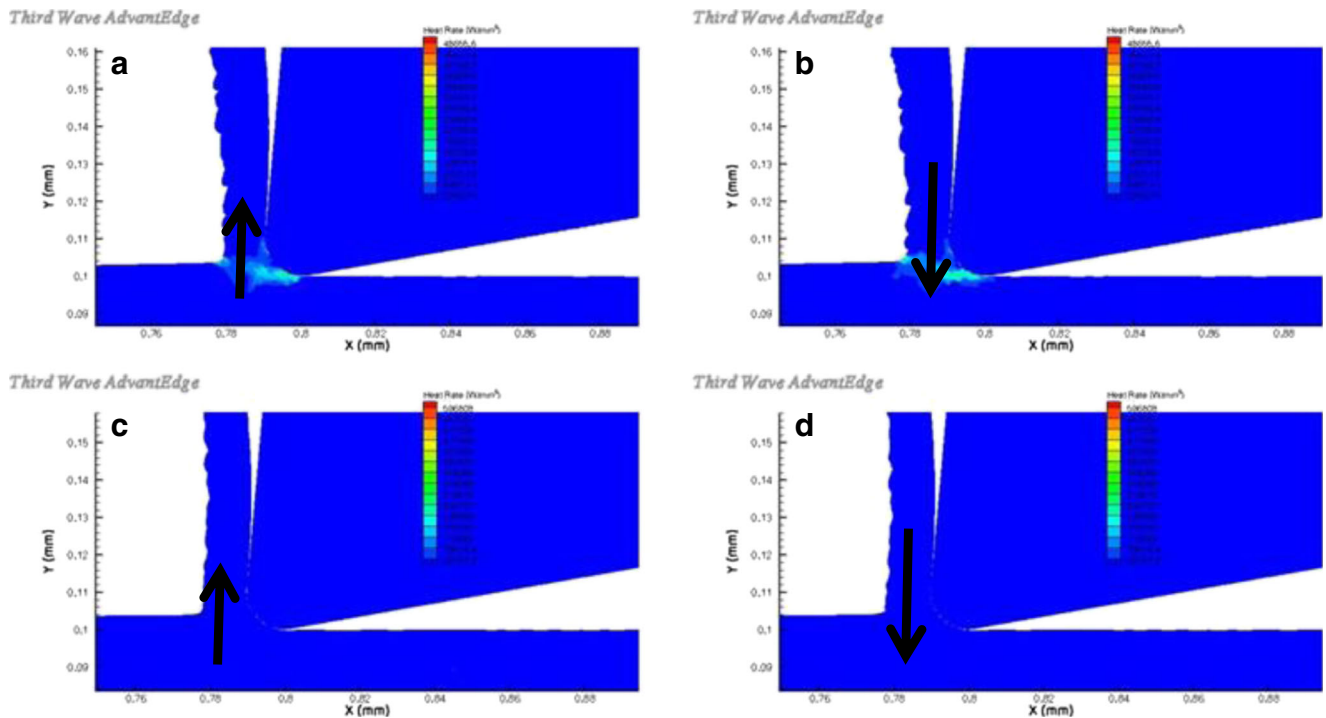
Fig. 21 The change in the direction of the heating rate for a 10-μm radius cutting tool operating at 100,000 rpm with a diamond cutting tool: **a** 10 μm feed/tooth when $F_C/F_T > 1$ (chip formation), **b** 10 μm feed/tooth when $F_C/F_T < 1$ (burr formation), **c** 5 μm feed/tooth when $F_C/F_T > 1$ (chip formation), and **d** 5 μm feed/tooth when $F_C/F_T < 1$ (burr formation)

Fig. 22 The change in the direction of the heating rate for a 4-μm radius cutting tool operating at 100,000 rpm with a diamond cutting tool: **a** 4 μm feed/tooth when $F_C/F_T > 1$ (chip formation), **b** 4 μm feed/tooth when $F_C/F_T < 1$ (burr formation), **c** 2 μm feed/tooth when $F_C/F_T > 1$ (chip formation), and **d** 2 μm feed/tooth when $F_C/F_T < 1$ (burr formation). The *arrows* show the direction of movement of the thermal field
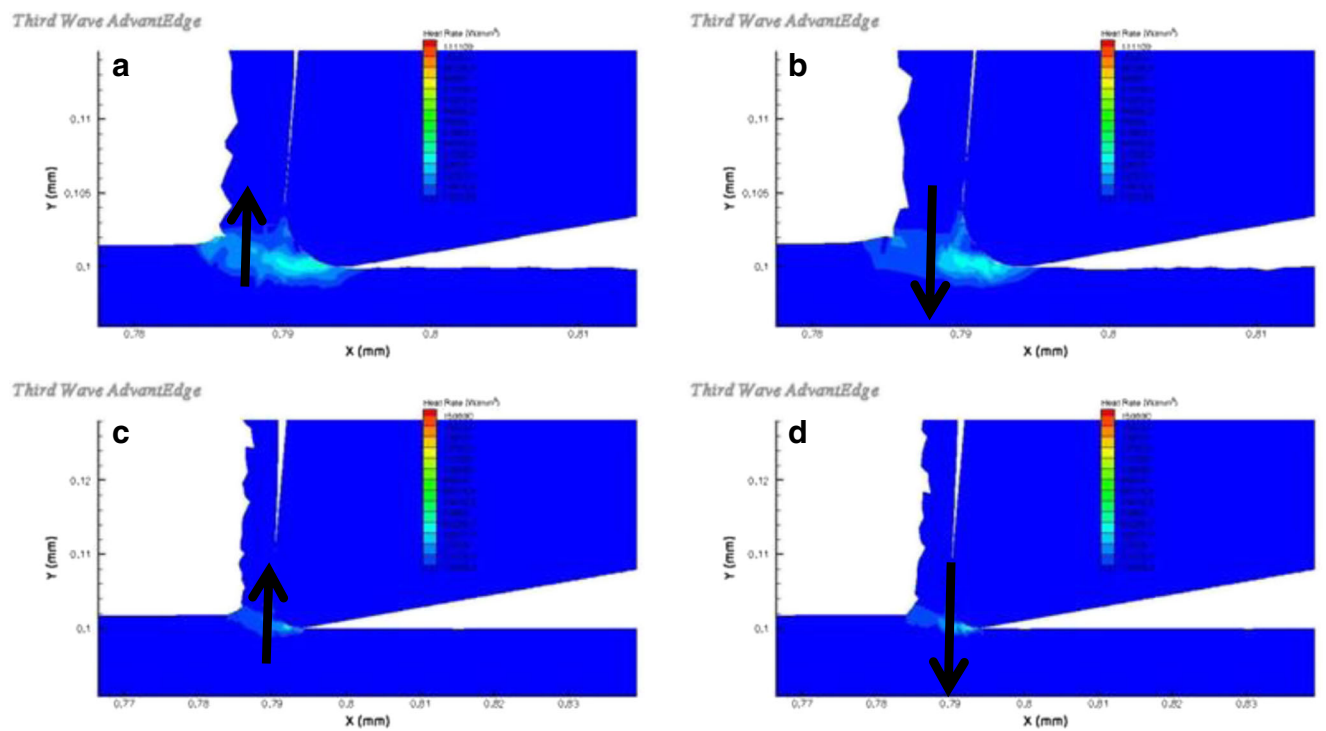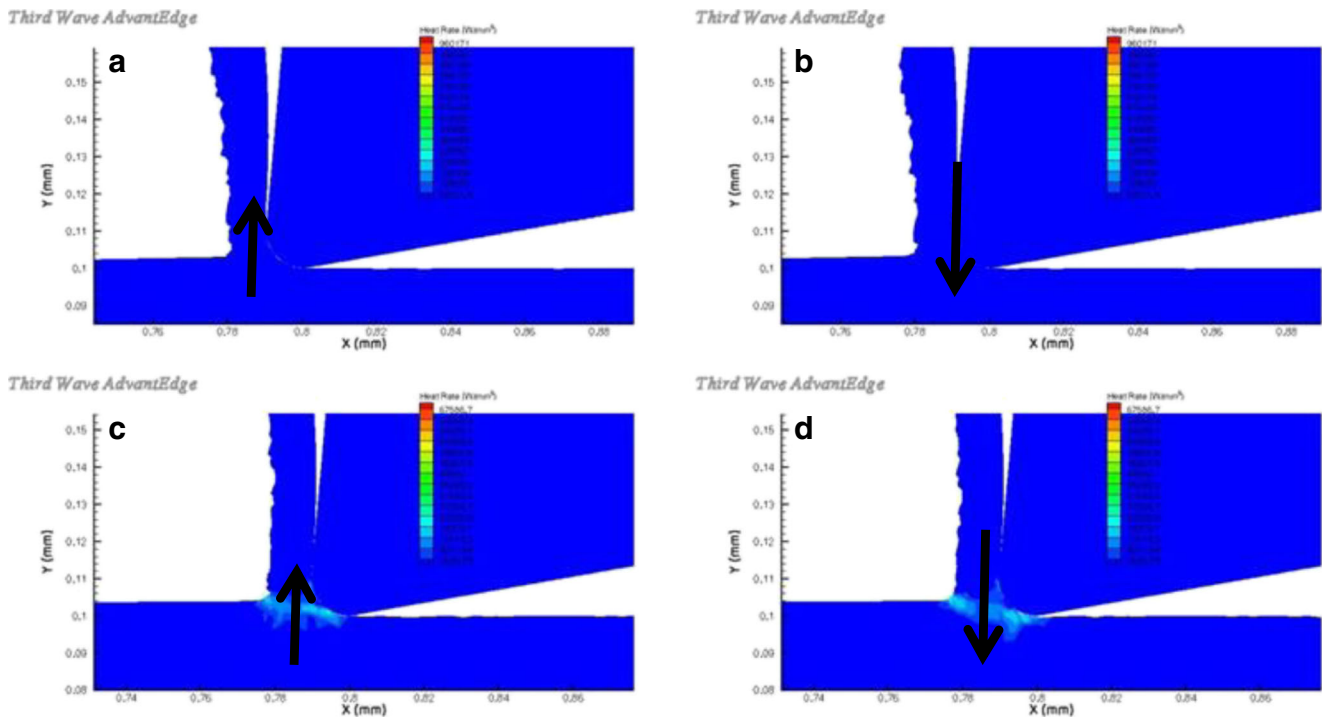
Fig. 23 The change in the direction of the heating rate for a 10-μm radius cutting tool operating at 150,000 rpm with a diamond cutting tool: **a** 10 μm feed/tooth when $F_C/F_T > 1$ (chip formation), **b** 10 μm feed/tooth when $F_C/F_T < 1$ (burr formation), **c** 5 μm feed/tooth when $F_C/F_T > 1$ (chip formation), and **d** 5 μm feed/tooth when $F_C/F_T < 1$ (burr formation). The *arrows* show the direction of movement of the thermal field

Fig. 24 The change in the direction of the heating rate for a 4-μm radius cutting tool operating at 150,000 rpm with a diamond cutting tool: **a** 4 μm feed/tooth when $F_C/F_T > 1$ (chip formation), **b** 4 μm feed/tooth when $F_C/$ $F_T < 1$ (burr formation), **c** 2 μm feed/tooth when $F_C/F_T > 1$ (chip formation), and **d** 2 μm feed/tooth when $F_C/F_T < 1$ (burr formation). The *arrows* show the direction of movement of the thermal field
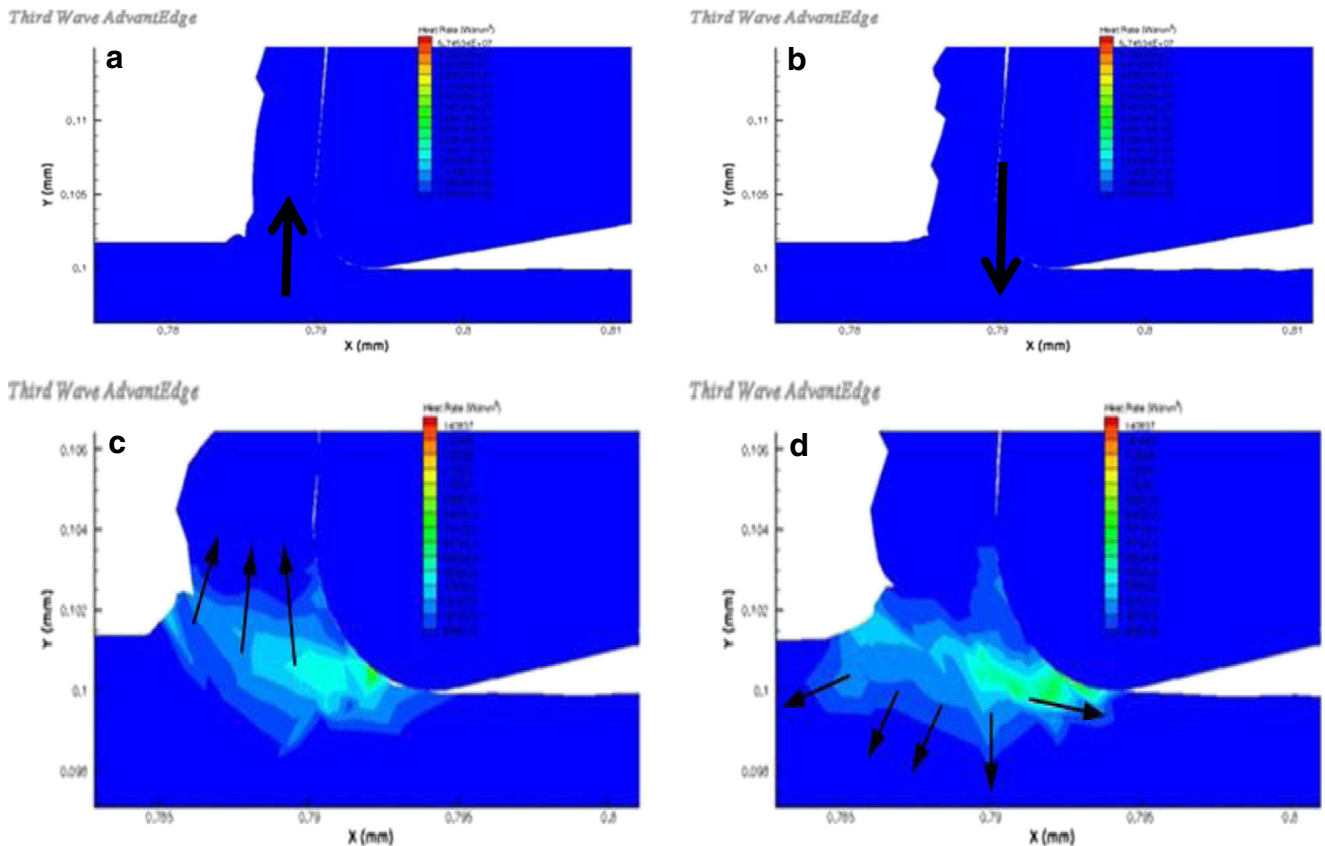
References

1. Chae J, Park SS, Freiheit T (2006) Investigation of micro-cutting operations. Int J Mach Tools Manuf 46:313–332
2. Dornfeld D, Min S, Takeuchi Y (2006) Recent advances in mechanical micromachining. Annals of CIRP 55(2):745–768
3. Backer WR, Marshall ER, Shaw MC (1952) The size effect in metal cutting. Transactions of the ASME 74:61–72
4. Larsen-Basse, J. and P.L.B. Oxley 1973, Effect of strain-rate sensitivity on scale phenomenon in chip formation, in Proceedings of the 13th International Machine Tool Design & Research Conference, Birmingham, UK, pp. 56–63
5. Kopalinsky, E.M. and P.L.B. Oxley 1984, Size effects in metal removal processes. In Proceedings of the Institute of Physics Conference Series number 70, Third Conference, Mechanical Properties at High Rates of Strain
6. Joshi SS, Melkote SN (2004) An explanation for the size-effect in machining using strain gradient plasticity. Trans ASME – J Manuf Sci Eng 126:679–684
7. Kim C-J, Mayor JR, Ni J (2004) A static model of chip formation in microscale milling. Trans ASME – J Manuf Sci Eng 126:710–718
8. Gurin, F.V. 1967, Metal cutting using diamond tools with ground cutting edges, Maschinostryenie, Moscow
9. Kragelsky, I.V., M.N. Dobychin, and V.S. Kombalov 1982, Friction and wear—calculations and methods. New York: Pergamon Press Inc.
10. L'Vov NP (1968) Determining the minimum possible chip thickness. Mach Tooling 40:45–46
11. Basuray PK, Misra BK, Lal GK (1977) Transition from ploughing to rubbing. Wear 43:341–349
12. Vogler MP, Devor RE, Kapoor SG (2004) On the modeling and analysis of machining performance in micro-endmilling, part I: surface generation. ASME J Manuf Sci Eng 126:685–694
13. Son SM, Lim HS, Ahn JH (2005) Effects of the friction coefficient on the minimum cutting thickness in micro cutting. Int J Mach Tools Manuf 45:529–535
14. Shimada S et al (1993) Feasibility study on ultimate accuracy in microcutting using molecular dynamics simulation. CIRP Ann 42:91–94
15. Yuan ZJ, Zhou M, Dong S (1996) Effect of diamond tool sharpness on minimum cutting thickness and cutting surface integrity in ultraprecision machining. J Mater Process Technol 62:327–330
16. Sun J, Guo YB (2009) Material flow stress and failure in multiscale machining titanium alloy Ti-6Al-4V. Int J Adv Manuf Technol 41:651–659
17. www.matweb.com. 1996-2016 [cited November 2016]; available from: http://www.matweb.com/
18. Blazynski TZ (ed) (1987) Materials at high strain rates. Elsevier Applied Science Publishers, London
19. Wu XY, Ramesh KT, Wright TW (2003) The effect of thermal softening and heat conduction on the dynamic growth of voids. Int J Solids Struct 40:4461–4478
20. Seo S, Min O, Yang H (2005) Constitutive equation for Ti-6Al-4 V at high temperatures measured using the SHPB technique. Int J Impact Eng 31:735–754
21. Khan AS, Suh YS, Kazmi R (2004) Quasi-static and dynamic loading responses and constitutive modeling of titanium alloys. Int J Plast 20:2233–2248
22. Henry SD, Dragolich KS, DiMatteo ND (1995) Fatigue data book: light structural alloys. ASM International, Ohio
23. Kang IS, Kim SK, Seo YW (2008) Cutting force model considering tool edge geometry for micro end milling process. J Mech Sci Technol 22:293–299
24. Barry J, Byrne G, Lennon D (2001) Observations on chip formation and acoustic emission in machining Ti-6Al-4 V alloy. Int J Mach Tools Manuf 41:1055–1070
25. Cotterell M, Byrne G (2008) Characterization of chip formation during orthogonal cutting of titanium alloy Ti6Al4V. CIRP J Manuf Sci Technol 1(2):81–85
26. Robinson, G. M., Wear of nanostructured coated cutting tools during mixed scale machining, 2007. Ph.D. thesis, Purdue University, West Lafayette, United States of America
27. Kim JD, Kim DS (1995) Theoretical analysis of micro cutting characteristics in ultra precision machining. J Mater Process Technol 49:387–398
28. Özel T, Zeren E (2007) Finite element analysis of the influence of edge roundness on the stress and temperature fields induced by high speed machining. Int J Adv Manuf Technol 35(3–4):255–267
29. Li R, Shih AJ (2006) Finite element modeling of 3D turning of titanium. Int J Adv Manuf Technol 29:253–261
30. Umbrello D (2008) Finite element simulation of conventional and high speed machining of Ti6Al4V alloy. J Mater Process Technol 196:79–87
31. Obikawa T, Usui E (1996) Computational machining of Ti alloy finite element modeling. Trans ASME J Manuf Sci Eng 118:208–215
32. Shi J, Liu RC (2004) The influence of material models on finite element simulation machining. Transactions of the ASME Journal of Manufacturing Science and Engineering 126:849–857
33. Usui E, Shirakashi T, Kitagawa T (1978) Cutting temperature and crater wear of carbide tools. Trans ASME J Eng Ind 100(2):236–243
34. Kitagawa T, Kubo A, Maekawa K (1997) Temperature and wear of cutting tools in high speed machining of Inconel 718 and Ti-6Al-6V-2Sn. Wear 202(2):515–525
35. Kim KW, Lee WY, Sin HC (1999) A finite element analysis of machining with the tool edge considered. J Mater Process Technol 86:45–55
36. Cao ZY, He N, Li L (2008) A finite element analysis of micro/meso scale machining considering the cutting edge radius. Applied Mechanics and Materials 10-12:631–636
37. Venkatesh V, Swain N, Srinivas G, Kumar P, Barshilla H (2016) Review on the machining characteristics and research prospects of conventional microscale machining operations. Mater Manuf Process 1–28. doi:10.1080/10426914.2016.1151045
38. Novakov T Computational analysis of micromachining Ti6Al4V titanium alloy (2010) Ph.D. thesis, Purdue University, West Lafayette, United States of America